Journal of Applied Physics TUTORIAL scitation.org/journal/jap

Electron dynamics in low pressure capacitively coupled radio frequency discharges

Cite as: J. Appl. Phys. **127**, 181101 (2020); doi: 10.1063/5.0003114
Submitted: 30 January 2020 · Accepted: 17 April 2020 ·
Published Online: 8 May 2020

View Online Export Citation CrossMark

S. Wilczek,[1,a)] J. Schulze,[1,2] R. P. Brinkmann,[1] Z. Donkó,[3] J. Trieschmann,[4] and T. Mussenbrock[4]

AFFILIATIONS

[1]Department of Electrical Engineering and Information Science, Ruhr University Bochum, D-44780 Bochum, Germany
[2]School of Physics, Dalian University of Technology, 116024 Dalian, China
[3]Institute for Solid State Physics and Optics, Wigner Research Centre for Physics, Konkoly-Thege Miklós str. 29-33, H-1121 Budapest, Hungary
[4]Electrodynamics and Physical Electronics Group, Brandenburg University of Technology Cottbus-Senftenberg, Siemens-Halske-Ring 14, D-03046 Cottbus, Germany

[a)]**Author to whom correspondence should be addressed:** sebastian.wilczek@rub.de. **URL:** https://www.tet.ruhr-uni-bochum.de/lehrstuhl/mitarbeiter/sebastian-wilczek/

ABSTRACT

In low temperature plasmas, the interaction of the electrons with the electric field is an important current research topic that is relevant for many applications. Particularly, in the low pressure regime ($\leq$10 Pa), electrons can traverse a distance that may be comparable to the reactor dimensions without any collisions. This causes "nonlocal," dynamics which results in a complicated space- and time-dependence and a strong anisotropy of the distribution function. Capacitively coupled radio frequency (CCRF) discharges, which operate in this regime, exhibit extremely complex electron dynamics. This is because the electrons interact with the space- and time-dependent electric field, which arises in the plasma boundary sheaths and oscillates at the applied radio frequency. In this tutorial paper, the fundamental physics of electron dynamics in a low pressure electropositive argon discharge is investigated by means of particle-in-cell/Monte Carlo collisions simulations. The interplay between the fundamental plasma parameters (densities, fields, currents, and temperatures) is explained by analysis (aided by animations) with respect to the spatial and temporal dynamics. Finally, the rendered picture provides an overview of how electrons gain and lose their energy in CCRF discharges.

I. INTRODUCTION

Low pressure capacitively coupled radio frequency (CCRF) discharges[1–4] play an enormous role for various applications of crucial societal relevance and broad impact. These range from the semiconductor industry to coating technologies and biomedical/environmental applications.[5–9] For instance, in semiconductor manufacturing, the generation of nanometer-sized structures for integrated circuits necessitates good quality of high-aspect-ratio trenches,[10–13] and consequently, the control of the radio frequency etching process must be optimized. For example, deep reactive-ion etching (DRIE)[14–17] is a very anisotropic dry etch process that can generate aspect-ratios in the range of 50:1 with almost 90 degree trench walls. This process can generate capacitor trenches for dynamic random access memories (DRAMs)[18] as well as conductor paths for 3D integrated circuit systems.[19] At the same time, radio frequency sputtering[20–22] as well as plasma enhanced chemical vapor deposition (PECVD)[23,24] become increasingly important to deposit high quality layers on a substrate. Among other applications, these processes are essential to deposit passivation layers inside a trench[25,26] in order to prevent the etching of sidewalls. Further exemplary areas of applications are protective layers for metallic components,[27–29] barrier films for synthetic products,[30–33] and deposition of amorphous and mono-crystalline silicon for the thin film solar cell fabrication.[34] These days, both etching and deposition processes reach the precision of single atomic layers.[35–37] In order to realize this high degree of process control and selectivity in Atomic Layer Etching (ALE) and Atomic Layer Deposition (ALD), a precise control of process relevant flux-

energy distribution functions of different particle species in the plasma volume and at boundary surfaces is required. Such control, in turn, requires a deep understanding of the spatiotemporal dynamics of various species in CCRF plasmas as a basis for knowledge based process optimization. Finally, a great variety of atmospheric pressure microplasmas are operated via capacitive coupling at radio frequencies,[38,39] e.g., microatmospheric pressure plasma jets[40–42] and some types of dielectric barrier discharges.[43] Also, in these systems, a knowledge based control of distribution functions based on fundamental insights into the spatiotemporal particle dynamics is required to improve applications such as wound healing, sterilization, and cancer treatment. Typically, this requires an optimization of the generation of process relevant radical densities. All these applications make CCRF discharges an indispensable technological tool, which requires a fundamental understanding in order to obtain a much better process control.

A. Discharge setup

Figure 1 shows a schematic of a typical setup of a capacitively coupled plasma,[1,2] which consists of two plane and parallel electrodes with circular surfaces that are installed in a vacuum chamber. The feedstock gases are injected at a certain position at the surface of the chamber or a showerhead is installed at the position of the electrode. The gases flow through the electrode gap and are pumped away by a vacuum pump. The types of feedstock gases range from simple noble gases, such as argon and neon, which are usually used for experimental studies as well as plasma sputtering applications, to highly complex gases,[44–50] such as O_2, N_2, SF_6, and CF_4, and their mixtures are used for etching processes in the microelectronic industry. The gas pressure is in the range of $0.01 < p < 10$ Pa, and the gas temperature is between $300 < T_g < 600$ K. Based on the ideal gas law,

$$p = k_B T_g n_g, \tag{1}$$

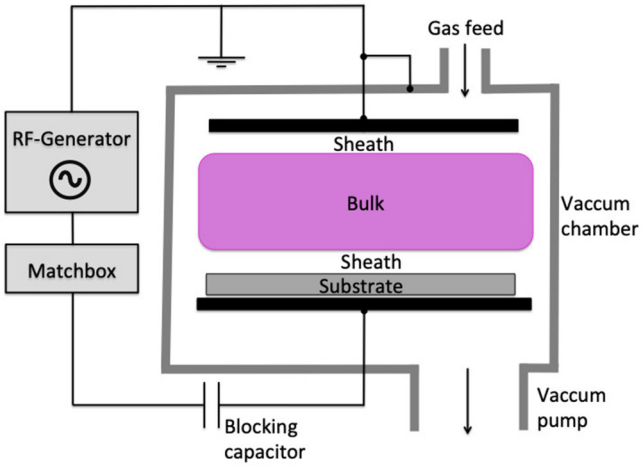

FIG. 1. Schematic of a CCRF discharge setup.

the resulting gas density varies between $10^{19} < n_g < 10^{21}$ m^{-3}. Here, k_B is the Boltzmann constant. In contrast, the electron and ion densities are several magnitudes lower, $10^{14} < n_{e,i} < 10^{16}$ m^{-3}. CCRF discharges at low pressures are operated in the low temperature plasma regime, where electrons have a high temperature, $1 < T_e < 5$ eV, and ions often have a temperature in the bulk plasma, which is similar to the gas temperature, $0.03 < T_i < 0.1$ eV ($T_e \gg T_i$). Most of the applications require a substrate holder on one electrode (the bottom electrode in Fig. 1) in order to deposit materials or to etch trenches. The used substrate frequently consists of a dielectric material, and the rf voltage drop across this material is small and can be neglected. The upper electrode as well as the vacuum chamber are grounded. In contrast, the electrode at the bottom position is connected via a blocking capacitor, and a matchbox to a radio frequency generator couples the power into the discharge. Typical radio frequencies are between $1 < f_{rf} < 100$ MHz. The matching network is important in order to match the impedance of the plasma to the impedance of the rf-generator. Typically, a sinusoidal radio frequency voltage is applied to the driven electrode, which has amplitudes in the range of 50 V $< V_0 <$ 10 kV. The blocking capacitor prevents the flow of a DC current in the circuit, and the voltage drop across it compensates the self-bias voltage over the plasma that forms in the presence of any discharge asymmetry. Such an asymmetry can originate from the unequal electrode surface areas: The grounded surface of the upper electrode and the reactor wall lead to the situation that the total grounded surface area A_g can be larger than the surface area of the powered electrode A_p. Consequently, the discharge becomes geometrically asymmetric and a DC self-bias is generated. For conducting electrodes, this voltage drop is easy to measure experimentally by a voltage probe and gives an appropriate orientation how geometrical asymmetric the discharge is.[51–53] In large area reactors, the electrode area ratio can be $A_g \approx A_p$. Therefore, the DC self-bias is negligible (in single-frequency unmagnetized CCRF discharges with identical surface materials), and the discharge along the axis is almost symmetric. The materials of different surfaces (substrate, electrode, reactor wall) play a very important role for the plasma-surface interaction.[54–59] For instance, the material of the electrode can be stainless steel, and the wafer at the substrate holder consists of SiO_2. Different materials in combination with different plasma species (neutrals, ions, and electrons) lead to highly complex plasma-surface models, which need to take into account energy dependent ion and electron induced secondary electron emission (SEE) coefficients as well as energy dependent particle reflection coefficients at the respective surface.

The most important part of such a CCRF discharge is the region between the electrodes. A quasi-neutral plasma bulk is generated in the center of the discharge. Most of the gas phase chemistry occurs in this region (generation of ions, radicals, and other molecules). In front of the electrodes, two positively charged layers arise, which are called plasma sheaths. In these regions, the positive charged particles (ions) are accelerated toward the adjacent electrode by an electric field and interact with the surface (sputtering or etching), while the negatively charged particles (generally electrons and in some cases also negative ions) are confined to the bulk by this field. The advantage of such a symmetric CCRF discharge compared to other plasma discharges (inductively coupled plasmas

or Hall thrusters) is the simple geometry of the planar two-electrode system. Consequently, most of the power is coupled into the plasma along the axial direction between the electrodes, which is a significant benefit for modeling such as a CCRF discharge (see Sec. II).

B. Background and goal of this work

The optimization of technological processes requires a fundamental knowledge of the electron dynamics in CCRF discharges. This is because the electrons are responsible for the generation of positive ions (ionization), which are accelerated toward a substrate where they interact with the surface materials and for the generation of radicals. In order to ionize the background gas, electrons need a certain energy. Therefore, one of the most fundamental questions in low pressure CCRF discharges is how do the electrons gain and lose their energy[60,61]? In the last few decades, this issue has been studied and called "electron heating." However, electron heating and electron power absorption are physically two different mechanisms. Electrons gain and lose their energy in an electric field, which has predominantly only one direction in CCRF discharges (perpendicular to the electrodes). Consequently, an ensemble of electrons with an isotropic velocity distribution function and a corresponding electron temperature, $T_{e,1}$, which passes through an electric field, becomes anisotropic. During this acceleration in the electric field, the electrons gain energy and power absorption occurs due to the anisotropic increase of the velocity. Heating occurs when the anisotropic distribution of the velocity components is redistributed in an isotropic manner by collisions with the neutral gas particles, which is called isotropization. Afterward, the ensemble of electrons underlies again an isotropic distribution with a new temperature $T_{e,2}$, which is higher than the previous temperature, $T_{e,2} > T_{e,1}$. Finally, the combination of electron power absorption in an electric field and the isotropization due to collisions is termed electron heating and is illustrated in Fig. 2. In the last few decades, two different types of electron heating mechanisms have been introduced. The first one is the collisional type of heating, which is traditionally modeled as "Ohmic heating."[1–3] However, in low pressure CCRF discharges, the collision probability is low and electrons traverse through the discharge without any collisions for a certain period. This means that isotropization is severely restricted. Godyak and co-workers[62,63] showed that an additional "collisionless heating" mechanism occurs at low pressures, which is named "stochastic heating." It is based on a time and space varying electric field, which in CCRF discharges is mainly related to the rf oscillating boundary plasma sheaths. The concept of this "heating" mechanism is illustrated in Fig. 3. The initial situation is that an electron with an individual energy ε penetrates into the plasma sheath. Due to the electric field that points toward the electrode, the electron will be reflected and will leave the plasma sheath with the same energy ε if the plasma sheath does not move (scenario A in Fig. 3). However, the plasma sheath region expands and collapses during a radio frequency cycle. Consequently, the electron is accelerated (scenario B, expanding sheath in Fig. 3) or decelerated (scenario C, collapsing sheath in Fig. 3) during the interaction with the moving plasma sheath.

The concept of this collisionless electron–field interaction is based on the "hard wall" model,[64–67] which, in turn, is related to

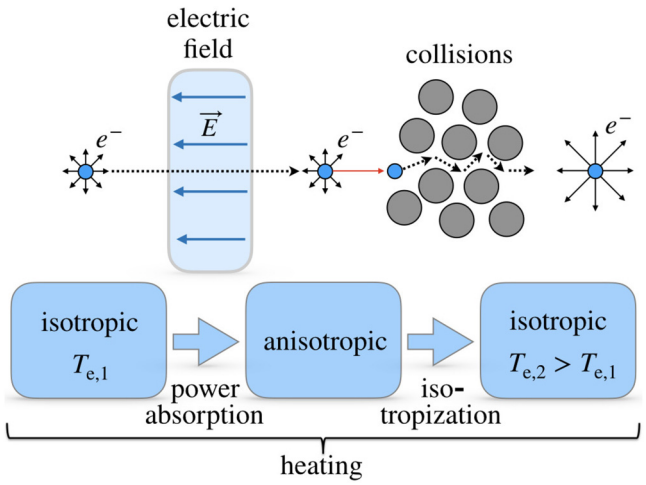

FIG. 2. A sketch of the concept of electron heating. The blue circle represents the ensemble of electrons and the gray circles represent the neutral background particles. First, the ensemble of electrons obeys an isotropic velocity distribution with a temperature of $T_{e,1}$. Second, the velocity distribution function becomes anisotropic due to an acceleration in an electric field along one particular direction. Third, the electron energy is redistributed to other directions by collisions, i.e., the anisotropy is reduced, and the ensemble of electrons again becomes isotropic but with a higher temperature ($T_{e,2} > T_{e,1}$).

"Fermi acceleration."[68] Fundamentally, collisionless or stochastic heating is only an acceleration process in which the time-varying electric field dissipates power to/from the electrons, but collisions are still necessary in order to isotropize the electron distribution.

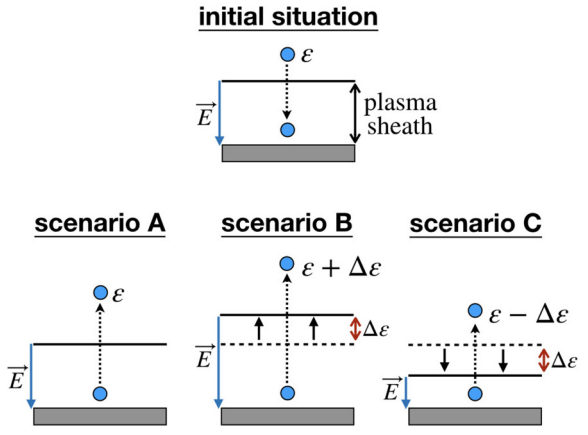

FIG. 3. A sketch of the concept of collisionless electron power absorption. Top: The initial situation, when an electron penetrates into a plasma sheath. Bottom: Three different scenarios. Scenario A: The plasma sheath does not move and the electron is reflected with the same energy. Scenario B: The plasma sheath expands and the electron is reflected with a higher energy. Scenario C: The plasma sheath collapses and the electron is reflected with less energy.

However, over the last few decades, the term "heating" has become established, and several fundamental studies based on theoretical, computational, and experimental work[1–3,62–65,67,69–77] have given many novel insights into the electron dynamics at low pressures. Most of these studies have used different terms such as collisionless, noncollisional, anomalous, stochastic, transit time, or sheath heating in order to describe the collisionless power dissipation to/from electrons, which, finally, all describe the same mechanism, the electron interaction with a space and time varying electric field. In addition to these pioneering works, further electron heating terminologies have been introduced and deeper understanding was conveyed; "nonlinear electron resonance heating" (NERH),[78–82] which is based on the excitation of the plasma series resonance (PSR),[83–89] pressure heating,[90–92] ambipolar heating,[44,93–96] Bounce-Resonance-Heating (BRH),[97–101] heating due to ion and electron induced secondary electrons,[54,55,102–104] and nonlinear wave–particle heating.[72,105–110] Besides these mechanisms in single-frequency rf discharges, electron heating in dual-frequency discharges has also been addressed.[111,112] In conclusion, there is a long list of various papers that aim to understand the complex electron heating at low pressure. Most of them only use a different terminology but frequently explain similar heating characteristics. However, what makes the electron dynamics in low pressure CCRF discharges so complicated in detail? The main reason is that the electron mean free path, λ_m, is comparable or larger than the characteristic length of a local electric field.[113,114] Electrons can traverse through regions with different local electric fields between collisions, and, consequently, their local velocity and energy distribution are no longer determined by the local and instantaneous field alone but by the distribution of the electric field at different locations and times. This so-called "nonlocal" regime[113–119,119–122] strongly influences the electron current density as well as the electron distribution function at an individual position and time, e.g., the electron velocity distribution function (EVDF) changes from an isotropic to an anisotropic distribution. In particular, during the phase of plasma sheath expansion, anisotropic EVDFs have been observed,[72,81,107] which are related to the formation of energetic electron beams generated during sheath expansion. Experimental studies based on phase resolved optical emission spectroscopy[123–128] as well as simulation results[80,97,108,129,130] have shown that these energetic electron beams are essential for the ionization process. Finally, the dynamics of these energetic electron beams, which represent only a small fraction of all electrons, dominate the ionization in the discharge at low pressure and have to be studied in detail to control and optimize the plasma process.

This tutorial does not intend to give an overview of the diversity of electron heating mechanisms but instead provide the reader a basic strategy on how to study the dynamics of electrons in low pressure CCRF discharges using a self-consistent particle-in-cell/Monte Carlo collisions (PIC/MCC) simulation method. The spatial and temporal dynamics of the fundamental plasma parameters, such as densities, electric fields, currents, and temperatures, are investigated by adopting a step-by-step approach. Animations available as a supplementary material shall be used to show how these parameters are connected to each others in order to understand their physical interplay. Some plasma parameters additionally show hidden dynamics that are often overlooked, and it will be illustrated where and when these are to be found. The presented diagnostic method is suitable for all CCRF discharges, which can be investigated by means of 1d3v PIC/MCC simulations. In this work, a universal electropositive CCRF discharge scenario is depicted, which includes most of the features of electron dynamics in the low pressure regime ($0.01 < p < 10$ Pa).

Based on this universal case, the following fundamental questions are addressed in this tutorial:

- How is the electric field distributed over space and time and how does it influence the electrons?
- How is current continuity ensured during the whole rf cycle?
- How does the electron energy distribution look like and which electrons are important to sustain the discharge via ionization?
- How is the electron temperature defined in such a low pressure regime and what is the difference between heating and dissipation?
- How do the collisional and collisionless electron power gain and loss dynamics really work?

This tutorial is structured in the following way: Sec. II introduces the modeling and the simulation of a capacitively coupled plasma. In Sec. III, spatiotemporal diagnostic methods illustrate the interplay between different plasma parameters in five subsections: In Subsection III A, the interplay between the plasma density and the electric field is presented. Subsection III B deals with different current densities with respect to current conservation. The dynamics of slow and fast electrons and the ionization and excitation rate are discussed in Subsection III C. The spatiotemporal dynamics of the electron temperature and the electron power absorption are illustrated in Subsection III D. Subsection III E introduces a concept how to distinguish between different electron power absorption mechanisms. Finally, in Sec. IV, conclusions are drawn.

II. MODELING AND SIMULATION

A. Modeling of low pressure CCRF discharges

In order to model CCRF discharges efficiently, some general deliberations are of use as to which physical effects must be taken into account and which simplifications can be adopted. Order-of-magnitude considerations show that, to a large extent, classical mechanics prevails. Relativistic effects can be ignored, even for the light electrons, since their kinetic energies are typically 1–1000 eV (and even under extreme conditions smaller than 10 keV), which is small compared to the rest energy $m_e c^2 = 511$ keV. To clarify the role of quantum mechanics, consider the separation between the atomic scales a (typical molecule diameter) and λ_{dB} (de Broglie wavelength), both below 10^{-9} m, and the average interparticle distances that are $l_g = n_g^{-1/3} \approx 10^{-7}$ m for the neutrals and $l_e = n_e^{-1/3} \approx 10^{-5}$ m for the charges. The relation $a \ll l_g$ ensures that the neutrals and the ions behave like ideal classical gases, and the relation $\lambda_{dB} \ll l_e$ ensures the same for the electrons. When particles get closer than a or λ_{dB}, quantum mechanics does play a role, but these events—seen as "collisions"—are isolated and do not contribute to the internal energy. This tutorial will concentrate on the dynamics of the charged particles, electrons and ions, with a focus on the former. The neutrals, in contrast, will be treated as a homogeneous background, which only provides collision partners.

Effects such as gas heating and gas depletion[48,131–134] or generation of fast neutrals[59,135,136] are thus neglected.

The charges are described by two complementary concepts, one is the ensembles of classical particles that obey Newton's equations of motion. A species index s is introduced, which here runs over e (electrons) and i (ions), and a particle index k that runs from 1 to N_s, the number of particles of species s. The ensemble model formulates a set of differential equations for the particle positions $\vec{r}$ and velocities $\vec{v}$, with "collisions" being a reminder of the interaction terms that must be discussed separately,

$$\frac{d\vec{r}_k}{dt} = \vec{v}_k, \tag{2}$$

$$\frac{d\vec{v}_k}{dt} = \frac{q_s}{m_s}\vec{E}(\vec{r}_k, t) + \text{"collisions."} \tag{3}$$

Here, $\vec{E}$ is the electric field, q_s the charge, and m_s the mass of species s. Often, no external magnetic field is applied in CCRF discharges, and electromagnetic effects,[137,138] such as the skin effect, play only a role in specific situations, depending on the reactor size, the plasma density, and the driving frequency. Therefore, in this work, the magnetic field is neglected. In addition to the equations of motion, the particle–field interaction is often based on Maxwell's equations in an electrostatic approximation,

$$-\nabla^2\Phi = \rho/\epsilon_0. \tag{4}$$

Here, $\Phi = \Phi(\vec{r}, t)$ is the electrostatic potential, ϵ_0 is the vacuum permittivity, and $\rho = \rho(\vec{r}, t) = e(n_i(\vec{r}, t) - n_e(\vec{r}, t))$ is the charge density assuming singly ionized gas atoms (molecules) and only positive ions, with e being the elementary charge. The gradient of the potential determines the electric field, $\vec{E} = -\nabla\Phi$. However, in addition to the field–particle interaction, the particle–particle interaction is a very fundamental process that leads to ionization, excitation, and momentum transfer between the particles. Plasma physics theory makes use of the concept of particle collisions, where energy dependent cross sections, $\sigma(\varepsilon)$, are applied to treat the particle–particle interaction. These cross sections are available on different databases,[139–141] e.g., LXCat.

The other fundamental description of charged particle species is based on the distribution function, $f = f(\vec{r}, \vec{v}, t)$. With respect to the dynamics of the particle–field and particle–particle interaction, the full evolution of the distribution function is described by the Boltzmann equation (BE),[1,2,142]

$$\frac{\partial f}{\partial t} + \vec{v}\cdot\nabla_{\vec{r}} f + \frac{q}{m}\vec{E}\cdot\nabla_{\vec{v}} f = \left.\frac{\partial f}{\partial t}\right|_c. \tag{5}$$

Here, $\left.\frac{\partial f}{\partial t}\right|_c$ represents the temporal change of the distribution function due to collisions and $\nabla_{\vec{v}}$ and $\nabla_{\vec{r}}$ are the gradients in the velocity and real space, respectively. This integro-differential equation is the fundamental one of almost every theoretical and simulation work, in order to solve for the distribution function and, consequently, for the full dynamics of charged particles. However, solving this equation is quite challenging, and most of the studies are based on approximations,[143–150] such as the two term approximation. In order to reduce the complexity of the BE, the moments of the Boltzmann equation[151–153] are introduced, which lead to the macroscopic conservation (fluid) equations.[1,2] These equations are useful to investigate the spatial and temporal dynamics of the charged particles by introducing macroscopic parameters[151,152] such as the particle density, the particle flux, the pressure, and the energy density. In general, these quantities are obtained from the velocity moments of the distribution function.

In this tutorial, the macroscopic quantities and equations are derived based on the symmetry properties of the CCRF discharge. As mentioned before, the electrodes are assumed to be planar and symmetric. In addition, the size of the electrodes is considered to be infinite, and, consequently, the system becomes axially symmetric (here, along the x-axis, which is perpendicular to the electrodes) and translational invariant in the y- and z-direction. Thus, the dimension of the distribution function is reduced,

$$f(x, y, z, v_x, v_y, v_z, t) \longrightarrow f(x, v_\parallel, v_\perp, t), \tag{6}$$

with x being the remaining spatial dimension, which is parallel to the axis of the system, $v_\parallel = v_x$ being the velocity parallel to the axis, and $v_\perp$ being the perpendicular velocity. The zeroth velocity moment of the distribution function, $f(x, v_\parallel, v_\perp, t)$, is

$$n = \int f\, d^3v. \tag{7}$$

Here, $n = n(x, t)$ is the particle density. The differential, $d^3v = 2\pi v_\perp dv_\perp dv_\parallel$, can be written in cylindrical coordinates due to the symmetry properties for this specific case. Next, the first moment is introduced,

$$\Gamma = nu = \int v_\parallel f\, d^3v, \tag{8}$$

where $\Gamma = \Gamma(x, t) = nu$ is the particle flux density and $u = u(x, t)$ is the particle mean velocity. Both the particle flux density as well as the mean velocity only have a parallel component. The perpendicular component is zero due to symmetry reasons. The second moment is divided into a parallel and a perpendicular component,

$$P_\parallel = mnu^2 + p_\parallel = \int m v_\parallel^2 f\, d^3v, \tag{9}$$

$$P_\perp = p_\perp = \frac{1}{2}\int m v_\perp^2 f\, d^3v. \tag{10}$$

$P_\parallel = P_\parallel(x, t)$ and $P_\perp = P_\perp(x, t)$ are the parallel and perpendicular pressure in the co-moving frame, respectively. Here, $p_\parallel = p_\parallel(x, t)$ and $p_\perp = p_\perp(x, t)$ are the parallel and perpendicular pressure, respectively,

$$p_\parallel = mn\left(\langle v_\parallel^2\rangle - u^2\right), \tag{11}$$

$$p_\perp = \frac{1}{2} mn\langle v_\perp^2 \rangle. \tag{12}$$

The angle brackets $\langle\rangle$ mean averaging over all particles. At this point, the hierarchy of the velocity moments is usually cut off, and the individual macroscopic conservation (fluid) equations are introduced. The particle conservation equation is obtained by integrating the BE over all velocities,

$$\frac{\partial}{\partial t} n + \frac{\partial}{\partial x} \Gamma = G - L. \tag{13}$$

Here, $G = G(x, t)$ is the particle source term and $L = L(x, t)$ is the particle loss term. Multiplying the BE by $v_\parallel m$ and integrating over all velocities results in the momentum conservation,

$$m \frac{\partial}{\partial t} \Gamma + \frac{\partial}{\partial x} P_\parallel = qnE - \Pi_c. \tag{14}$$

Here, $\Pi_c = \Pi_c(x, t)$ is the change in momentum due to collisions. Multiplying the BE by $\left(\frac{1}{2} m v_\parallel^2 + \frac{1}{2} m v_\perp^2\right)$ and integrating again over all velocities, the contracted energy conservation equation is obtained,

$$\frac{\partial}{\partial t} w + \frac{\partial}{\partial x} Q = q\Gamma E - \varepsilon_c. \tag{15}$$

Here, $w = w(x, t) = \frac{1}{2}(P_\parallel + 2P_\perp)$ is the total energy density, Q is the energy flux, and $\varepsilon_c = \varepsilon_c(x, t)$ is the energy loss due to collisions. The conservation equations (13)–(15) describe the complete particle dynamics without any approximations. However, in every equation, a new quantity arises (Γ, $P_\parallel$, $P_\perp$, Q), which leads to an infinite hierarchy of differential equations. In particular, fluid simulations[154–159] truncate this hierarchy of equations and make use of an approximation; e.g., the drift-diffusion approximation with the assumption of an isotropic pressure and inertia terms are neglected. Fluid simulations clearly show their potential at high pressures and complex chemistry (a huge amount of different species). However, in low pressure CCRF discharges, kinetic dynamics, such as nonlocal and nonlinear[113–119,119–122] effects, play a very important role, and any kind of approximation causes substantial errors, especially regarding a correct description of the electron dynamics. Therefore, the distribution function has to be obtained. This is only possible by using spatially resolved particle simulation methods, which are usually based on the Monte Carlo method.[160–167]

B. Particle-in-cell/Monte Carlo collision simulation

The most commonly used particle simulation method for CCRF discharges is the particle-in-cell/Monte Carlo collision (PIC/MCC) method.[168–173] This simulation technique resolves the distribution function dynamics, which is analogous to solving the BE. Therefore, the full particle dynamics (including nonlocal and nonlinear dynamics) can be studied with respect to the particle–particle as well as the particle–field interaction. In order to resolve the temporal dynamics of the distribution function, a time step Δt is introduced, and a time discretization is applied for Eqs. (2)–(4). The concept of the PIC/MCC method is based on three general approaches: the first approach is the implementation of a numerical grid, with the size of a grid cell Δx. The equations of motion (2) and (3) as well as Poisson's equation (4) are solved on this grid to obtain the spatial information. This avoids including the particle–field interaction of individually charged particle pairs, such as Coulomb (electron–electron) collisions.[174,175] The second approach is the introduction of "super-particles" in order to reduce the computational effort drastically. Instead of solving the trajectory for N_{real} realistic particles, a computational weight, w_{sp}, assigns several real particles to a single super-particle, i.e., the number of superparticles, N_{sp}, relates to the number of realistic particles as $N_{\text{real}} = w_{\text{sp}} \cdot N_{\text{sp}}$. The third idea is related to the question of how to handle particle–particle interactions with respect to collisions. For this concept, the null-collision scheme[176,177] is used in this PIC/MCC simulation. This scheme calculates the probability, P_{col}, of a collision between charged particles and the background gas. In this work, the Phelps argon cross sections[141,178] are taken into account, which are well established and frequently used in simulation work.[13,20,71,76,80–82]

Figures 4 and 5 show the cross sections for electron–argon neutral and ion–argon neutral collisions, respectively. Three electron-neutral collisions (elastic, excitation, and ionization scattering) and two ion-neutral collisions (isotropic and backward scattering in the center-of-mass coordinate frame) are considered. The introduction of these general approaches leads to constraints with respect to physical and numerical parameters,[173]

- the Debye length, $\lambda_D = \sqrt{\frac{\epsilon_0 T_e}{e n_e}}$, must be resolved by the size of a grid cell; $\lambda_D \geq 2\Delta x$,
- the time step has to resolve the electron plasma frequency, $\omega_{\text{pe}} = \sqrt{\frac{e^2 n_e}{\epsilon_0 m_e}}$, by the following condition: $\omega_{\text{pe}} \Delta t \leq 0.2$,
- the Courant condition has to be fulfilled: $v_{\text{max}} \Delta t \leq \Delta x$, with v_{max} being the maximum velocity of a charged particle,

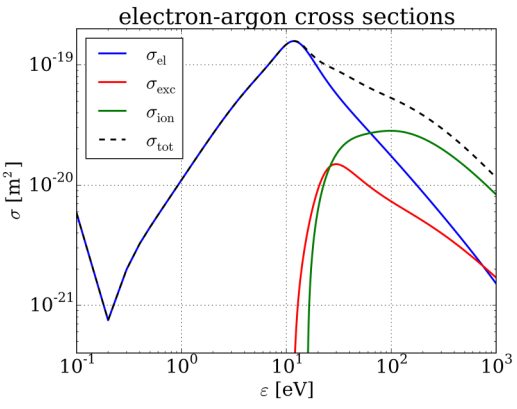

FIG. 4. The cross sections for electron–argon neutral collisions as a function of the electron energy, ε: elastic collision (blue line), σ_{el}; excitation (red line), σ_{exc}; ionization (green line), σ_{ion}; and the total cross section (black dashed line), σ_{tot}. Cross sections are taken from the Phelps database.[141]

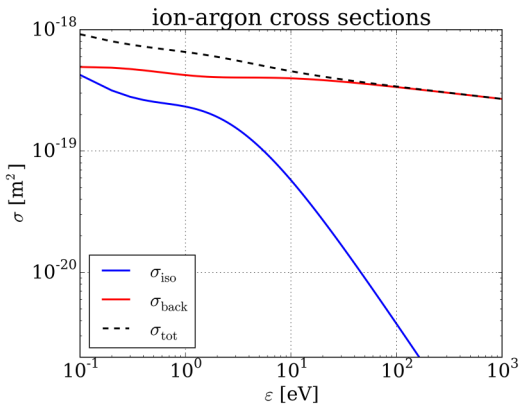

FIG. 5. The cross sections for ion–argon neutral collisions as a function of the ion energy (center-of-mass frame), ε: isotropic scattering (blue line), σ_{iso}; backward scattering (red line), σ_{back}; and the total cross section (black dashed line), σ_{tot}. Cross sections are taken from the Phelps database.[141,178]

- a sufficient number of super-particles must be present within one grid cell, and the number of super-particles within a Debye sphere should be reasonably high ($N_D \gg 1$[179,180]), and
- the probability of more than one collision of the same particle per time step should be small $\nu_{e,i}\Delta t \ll 1$, where $\nu_{e,i}$ is the collision frequency for electrons and ions, respectively.

As long as these stability and accuracy conditions are fulfilled, PIC/MCC simulations yield the distribution function self-consistently, and the electron and ion dynamics are treated kinetically. Additionally, the moments of the Boltzmann equations (13)–(15) can be calculated from the simulation without any approximation. This makes PIC/MCC simulations a powerful tool, which is used in this work to illustrate the intricacy of electron dynamics in low pressure CCRF discharges.

C. Simulation setup

Starting from the reactor shown in Fig. 1, first, the spatial dimensions are reduced from 3D to 1D. The one dimension, henceforth the x-coordinate, is perpendicular to the electrode surfaces (see Fig. 6). The particles move in a 3D velocity space with a cylindrical symmetry. This dimensional reduction leads to the abbreviation "1d3v PIC/MCC" simulation. As an exemplary scenario, the electrode gap size is set as $L_{gap} = 50$ mm and the electrodes are assumed to be infinite, planar, and parallel. The electrode at $x = 50$ mm is grounded, and the electrode at $x = 0$ is connected to a voltage source that provides the following waveform:

$$V_{rf}(t) = V_0 \sin(2\pi f_{rf} t). \tag{16}$$

Here, $V_0 = 500$ V is the voltage amplitude and $f_{rf} = 13.56$ MHz is the applied driving frequency. This voltage source represents the rf-generator. Since the discharge is considered to be symmetric, the blocking capacitor can be omitted in the simulation because no DC self-bias is generated.

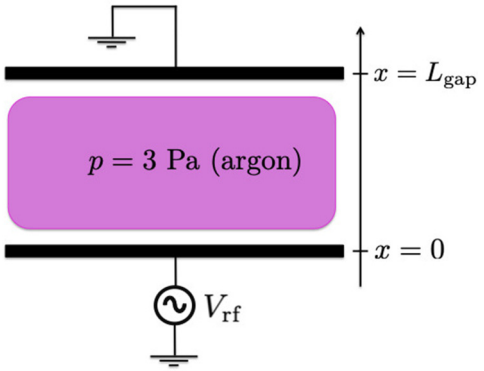

FIG. 6. A simplified schematic of the CCRF discharge that is used in the PIC/MCC simulation.

The background gas is argon with a temperature of $T_g = 300$ K and a pressure of $p = 3$ Pa. In this work, no realistic plasma-surface models are included. The emission of secondary electrons ($\gamma = 0$, $\delta = 0$) as well as the reflection (electron sticking $s = 1$) of particles at the electrodes are neglected in order to simplify the discussion of the electron dynamics. We would, however, like to point out that such realistic plasma-surface models exist and have recently been included in PIC/MCC simulations of CCRF discharges by considering material specific and energy dependent secondary electron emission coefficients due to ion, fast neutral, and electron impact at boundary surfaces. Energy and material specific electron reflection probabilities have been included as well.[54,104] The number of time steps per rf cycle is $N_{tspc} = 4000$, and the number of grid cells is $N_{cells} = 1000$ in order to fulfill the stability conditions. For reliable results, the number of super-particles for each species is in the range of $N_{sp} = 300\,000$, and the acquired data are averaged over 100 000 cycles after the convergence is achieved. The 1d3v electrostatic PIC/MCC code has been benchmarked against other implementations.[181]

III. RESULTS: ELECTRON DYNAMICS

In this section, the fundamental electron dynamics of a CCRF plasma at low pressure are discussed. PIC/MCC simulations of the specific discharge conditions, outlined in Table I, yield very universal features, which frequently occur in low pressure CCRF discharges.

First, basic plasma parameters, such as the plasma density, charge density, potential, and electric field, are discussed with respect to the temporal dynamics of the applied voltage in Subsection III A. In Subsection III B, the different current densities (electron, ion, displacement, and total current) are investigated with respect to current conservation. Subsection III C examines the energy distribution of electrons and demonstrates the critical approach of the thermodynamic concept of the electron temperature based on a Maxwellian distribution. Additionally, the motivation is to separate the electrons into two groups with different energies [slow ($\varepsilon < 15$ eV) and fast ($\varepsilon > 15$ eV) electrons]. Based on this idea, the correlation between fast electrons (electron beams)

TABLE I. The input parameters for the base case that considers symmetric, plane, and infinite electrodes in a single-frequency CCRF argon discharge.

Parameter	Value	Unit
Gas pressure (p)	3	Pa
Gas temperature (T_g)	300	K
Voltage amplitude (V_0)	500	V
Driving frequency (f_{rf})	13.56	MHz
Electrode gap size (L_{gap})	50	mm
Ion induced SEE coefficient (γ)	0	…
Electron induced SEE coefficient (δ)	0	…
Electron sticking coefficient (s)	1	…

and the excitation as well as ionization processes is shown. In Subsection III D, a distinction is made for the terminology "electron heating" and "electron power absorption." In this regard, the concept and the kinetic origin of the electron temperature are presented based on the parallel and perpendicular pressure. Finally, in Subsection III E, a diagnostic method based on the momentum balance equation (14) is introduced in order to clarify how electrons gain and lose their energy in CCRF discharges at low pressure. It is important to note that most of the following figures are temporal snapshots of animations, which can be watched by using the link below the figures. On the left side of these figures, spatiotemporal results of various plasma parameters are shown as a function of time over one rf cycle and as a function of the position between the electrodes. However, the resulting contour plots are frequently difficult to study, e.g, due to hidden features caused by the high range of the color map. Therefore, a temporal snapshot of the respective parameter as a function of the position is shown on the right side, which evolves as a function of time in the animation.

A. Basic plasma parameters

1. Plasma sheath and bulk

Starting with a thought experiment that does not take power coupling from the imposed electric field to the charged particles into account, three essential regions arise in a plasma, which is confined by two electrodes: the bulk and two sheath regions near each electrode (see Fig. 1). The reason for this is the difference between the thermal velocity of the electrons ($\sqrt{T_e/m_e}$) and the ions ($\sqrt{T_i/m_i}$). Due to the fact that electrons are much lighter than ions ($m_e \ll m_i$) and, with respect to the field of low temperature plasmas, the electron temperature is much higher than the ion temperature ($T_e \gg T_i$), electrons move faster to both electrodes and are quickly lost at the electrodes. Because of the resulting charge difference, a positive potential with respect to the electrode potentials is formed in the quasi-neutral plasma bulk. Consequently, an electric field is generated, which points toward the adjacent electrode and confines the electrons in the discharge. The slow ions are accelerated to the electrodes, and a plasma sheath is formed near both electrodes.[1,2] However, the sheath and bulk regions will decay if the power coupling into the discharge is not considered.

2. Power coupling into the plasma

In a capacitively coupled discharge, the radio frequency power is adjusted at the rf-generator and is coupled via a matchbox into the plasma (see Fig. 1). If the matching network operates correctly, the voltage at the powered electrode is almost perfectly sinusoidal. CCRF discharges are voltage driven systems; consequently, the rf current $I_{rf}(t)$ is self-adjusted and can be considered as an output signal of the plasma system. In a voltage driven system, higher harmonics in the rf current can be generated. Previous work[82] has shown that using a sinusoidal current as an input signal is a critical approach because these harmonics cannot exist if the current is forced to be sinusoidal. Based on these global input and output parameters, the question arises as to how does the interplay work between the very fundamental plasma parameters, such as the electron and ion density, $n_e(x, t)$ and $n_i(x, t)$; the charge density, $\rho(x, t)$; the potential, $\Phi(x, t)$; and the electric field, $E(x, t)$? The spatial and temporal distributions of these fundamental parameters are particularly important in order to understand the physics of the discharge on a nanosecond timescale.

3. RF voltage and current at the driven electrode

Figure 7(a) (Multimedia view) shows the rf voltage (blue line), $V_{rf}(t)$, and the rf current density (red line), $j_{rf}(t)$, at the powered electrode, $x = 0$ mm, as a function of time for one rf cycle ($T_{rf} = 1/f_{rf}$). These parameters can be easily measured in an experiment via current and voltage probes.[182,183] The sinusoidal voltage is an input of the PIC/MCC simulation [Eq. (16)]. The rf current density at the electrode is the output of the CCRF system and exhibits a nearly sinusoidal waveform at the given conditions. In experimental systems, the measured parameter is a current, $I_{rf} = j_{rf}A$. However, in 1d3v PIC/MCC simulations, both electrode surfaces, A, are assumed to be infinite; therefore, only a current density makes sense to be discussed. In such a low pressure regime, the impedance of the discharge approximates that of a capacitor. The consequence of this is that the rf current leads the rf voltage with a phase shift of $\varphi \approx 88°$. A phase shift of 90° would represent a purely capacitive impedance, which means no power is dissipated into the discharge, and, consequently, the plasma would decay. Therefore, the ≈2° difference from 90° is essential in order to put sufficient energy into the electrons to undergo collisions, such as ionization.

4. Interplay of the plasma parameters

The interplay of these fundamental plasma parameters is based on the nature of Maxwell's equations in an electrostatic approximation [Eq. (4)]. The difference of the ion, $n_i = n_i(x, t)$, and electron, $n_e = n_e(x, t)$ [Fig. 7(b) (Multimedia view)], densities creates a charge density [Figs. 7(c) and 7(d) (Multimedia view)],

$$\rho = e(n_i - n_e). \tag{17}$$

The potential, $\Phi = \Phi(x, t)$, [Figs. 7(e) and 7(f) (Multimedia view)] is calculated according to Poisson's equation,

$$-\frac{\partial^2 \Phi}{\partial x^2} = \rho/\epsilon_0. \tag{18}$$

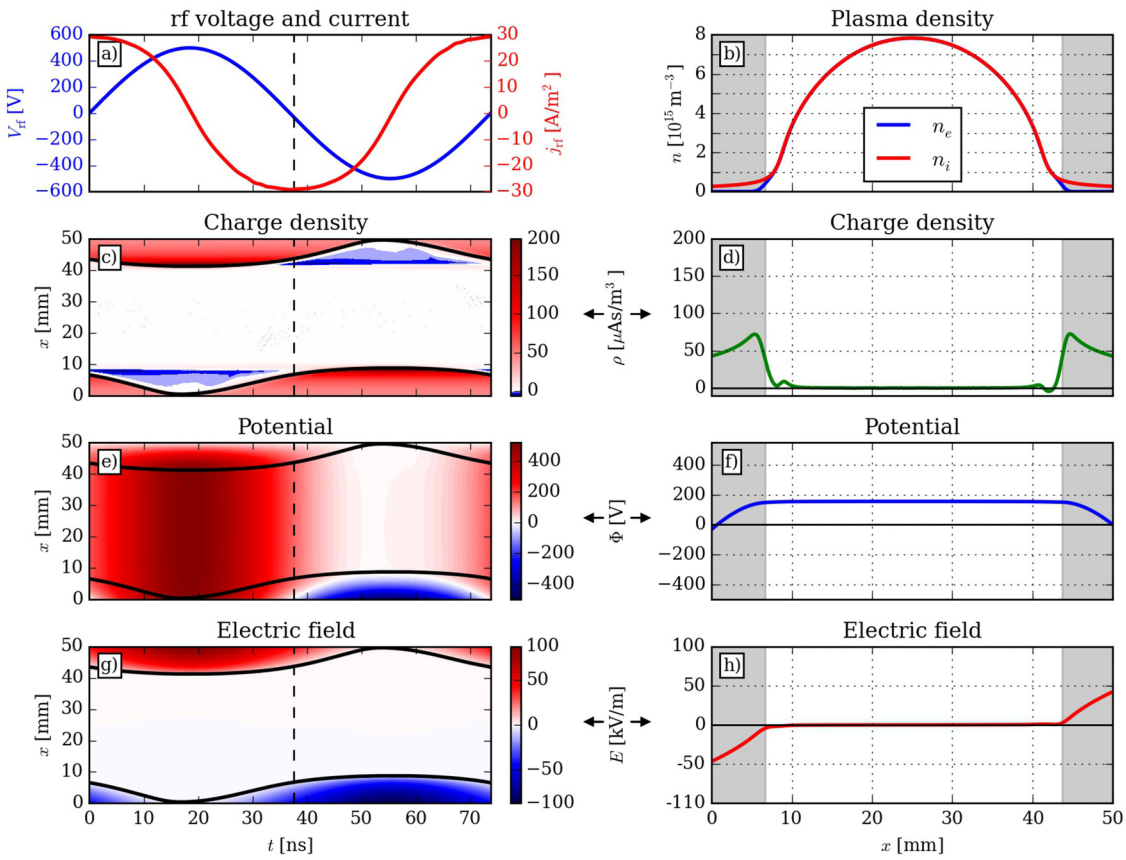

FIG. 7. (a) The rf voltage (blue) and the rf current density (red) at the driven electrode, (b) the electron and ion density profile, (c) and (d) the charge density, (e) and (f) the potential, and (g) and (h) the electric field. The left side presents spatiotemporal results, the solid black lines indicate the electron sheath edges, and the vertical black dashed line represents the time that is related to the temporal snapshot on the right side. The gray areas on the right side indicate the plasma sheaths. The color bars indicate the absolute values. Discharge conditions: argon gas, $p = 3$ Pa, $V_0 = 500$ V, $f_{rf} = 13.56$ MHz, $L_{gap} = 50$ mm. The animation available as a supplementary material shows the full dynamics. Multimedia view: https://doi.org/10.1063/5.0003114.1.

Consequently, the electric field, $E = E(x, t)$, [Figs. 7(g) and 7(h) (Multimedia view)] is obtained by

$$E = -\frac{\partial \Phi}{\partial x}. \tag{19}$$

5. Spatial distribution

The main features of the spatial distributions occur in three different regions, the plasma sheath at the powered electrode [$0\,\text{mm} < x < s_p(t)$], the plasma bulk [$s_p(t) < x < s_g(t)$], and the plasma sheath at the grounded electrode [$s_g(t) < x < 50\,\text{mm}$], where $s_{p,g}(t)$ are the electron sheath edge positions at the powered and grounded electrode, respectively. The sheath width is always represented by the gray areas in the right plots of Fig. 7 (Multimedia view), which is time modulated in the corresponding animation and by the black solid lines in the contour plots on the left side in Fig. 7 (Multimedia view). It is calculated as a function of time (taking as an example the powered electrode situated at $x = 0$) according to the following criterion:[184]

$$\int_0^{s(t)} n_e dx = \int_{s(t)}^{L_{gap}/2} (n_i - n_e) dx. \tag{20}$$

In the plasma bulk, quasi-neutrality is an adequate approximation ($n_e \approx n_e$); i.e., the red and blue lines in Fig. 7(b) (Multimedia view) overlap. Therefore, the charge density in Figs. 7(c) and 7(d) (Multimedia view) as well as the electric field in Figs. 7(g) and 7(h) (Multimedia view) in this region are very low, but not zero. The potential in Figs. 7(e) and 7(f) (Multimedia view) shows in this bulk region that a bulk potential, $\Phi_b(t)$, is self-adjusted during the full rf cycle, which must be always higher than the potential at the electrodes to confine the electrons inside the discharge. The profile of

the density in the plasma bulk is a classical ambipolar diffusion profile,[1,2] which is maintained by an ionization source.

In contrast to the plasma bulk, both plasma sheaths indicate significant temporal dynamics over the full rf cycle. The animation in Fig. 7(b) shows that only the electron density oscillates during the rf cycle in the plasma sheaths. Ions cannot follow the temporal change of the applied rf voltage due to their inertia; consequently, they only react to the time average of the electric field. Most of the applications of CCRF discharges operate in this radio frequency regime,

$$\omega_{pi} \ll \omega_{rf} \ll \omega_{pe}. \tag{21}$$

Here, ω_{pi} is the ion plasma frequency, ω_{pe} is the electron plasma frequency, and $\omega_{rf} = 2\pi f_{rf}$ is the applied radio frequency multiplied by the factor 2π in order to compare these angular frequencies. The strong decay of the density profiles inside the sheath is no longer related to diffusion but based on Boltzmann's relation[1,2] for the electrons and based on the acceleration along the sheath electric field for the ions.

6. Temporal dynamics

Almost the full rf voltage drops across the plasma sheaths and, thus, the pronounced temporal dynamics happen only in the sheath region. In order to explain the temporal evolution over one rf cycle, four characteristic times (t_1, t_2, t_3, and t_4) are defined in Table II, which are related to the minima, maxima, and the zero crossing of the rf voltage and current density in Fig. 7(a) (Multimedia view).

At the time, $t = t_1 = 0$ ns, the rf voltage is $V_{rf}(t_1) = 0$ V and the rf current is very close to a maximum of $j_{rf}(t_1) \approx 30$ A/m^2 due to the phase shift of $\varphi \approx 88°$. Both plasma sheaths indicate the same size, $s_p(t_1) = L_{gap} - s_g(t_1) \approx 6.5$ mm. Thus, the voltage drop shows the same magnitude but with opposing directions [see Figs. 7(e) and 7(f) (Multimedia view)]; i.e., the sheath electric field is negative in front of the powered electrode ($x = 0$ mm), and it is positive in front of the grounded electrode ($x = 50$ mm) [see Figs. 7(g) and 7(h) (Multimedia view)]. Therefore, the net voltage drop across the plasma is zero.

During the time interval $t_1 < t < t_2$, the rf voltage increases and the rf current decreases. Consequently, the voltage drop across the sheath at the grounded electrode ($x = 50$ mm) increases, and only the electrons react to this temporal voltage change. At the grounded electrode, the electric field increases and pushes the electrons away from the electrode. This leads to a stronger depletion of electrons near the grounded electrode, and, therefore, the width at the grounded electrode becomes larger and the local charge density increases. These sheath dynamics are part of the so-called sheath expansion phase at the grounded electrode ($x = 50$ mm) at $t = t_2 = 18.9$ ns. At this time, the maximum applied rf voltage of $V_{rf}(t_1) = 500$ V drops almost completely across the sheath at the grounded electrode, and the charge density as well as the electric field reach their local maximum.

At the opposing sheath ($x = 0$ mm), the voltage drop decreases and the opposite trend is observed. The sheath width, s_p, decreases because the population of electrons near the powered electrode increases [see Fig. 7(b) (Multimedia view)]. The resulting electric field in this sheath decreases, and it pushes the electrons less efficiently back into the bulk. This temporal phase is called the collapsing sheath phase. At $t = t_2 = 18.9$ ns, the sheath at the powered electrode is fully collapsed, and the local potential drop, the electric field, and the charge density reach a minimum. However, the voltage drop in the sheath is not zero; otherwise, too many electrons would leave the discharge. An rf floating potential, $\Phi_f \approx 10.5$ V, is self-adjusted in order to control the electron flux, $\Gamma_{e,p}$, at the powered electrode.

In every CCRF discharge, the flux of electrons Γ_e and ions Γ_i at either electrode must compensate each other over the full rf period in order to ensure that the plasma does not charge up,

$$\int_0^{T_{rf}} \Gamma_e(t)dt = \int_0^{T_{rf}} \Gamma_i(t)dt. \tag{22}$$

Figure 8 shows the time-dependence of the electron and ion fluxes at the powered (solid lines) and grounded (dashed lines) electrode. The ion flux (red lines) is small compared to the electron flux, but it is constant over time because ions see the time-averaged electric field. The electron flux shows a peak at the powered electrode ($x = 0$ mm) during the time of the fully collapsed local sheath ($t \approx t_2 = 18.4$ ns) and at the grounded electrode ($x = 50$ mm) during the time of the fully collapsed local sheath ($t \approx t_4 = 55.3$ ns).

TABLE II. Four characteristic times that represent the maxima, the minima, and the zero crossing in Fig. 7(a) (Multimedia view).

	t(ns)	t/T_{rf}	$V_{rf}(t)$	$j_{rf}(t)$
t_1	0	0	0	max
t_2	18.4	1/4	max	0
t_3	36.9	1/2	0	min
t_4	55.3	3/4	min	0

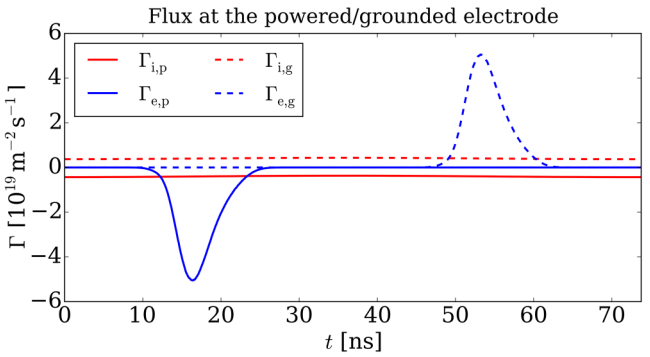

FIG. 8. The ion (red lines) and the electron flux (blue lines) at the powered (solid lines) and grounded (dashed lines) electrode as a function of time over one rf cycle. Discharge conditions: argon gas, $p = 3$ Pa, $V_0 = 500$ V, $f_{rf} = 13.56$ MHz, $L_{gap} = 50$ mm.

During the remaining time, the electron flux to the respective electrode is effectively zero.

During the time interval $t_2 < t < t_4$, the phase of sheath expansion takes place at the powered electrode ($x = 0$ mm). The increasing absolute value of the electric field in the sheath pushes the electrons away, which leads again to an electron depletion, and, therefore, the local electron sheath width, s_p, increases. At the same time at the opposing electrode ($x = 50$ mm), the collapsing sheath phase occurs, and the decrease of the sheath width, the electric field, and the charge density is illustrated in Fig. 7 (Multimedia view). At $t_3 = 36.9$ ns, one half of the sheath expansion phase at the powered electrode and one half of the sheath collapse phase at the grounded electrode are over, and the rf voltage is again $V_{rf}(t_3) = 0$ V and the rf current has a minimum at $j_{rf}(t_3) \approx -30$ A/m^2. This leads to a similar situation compared to the time t_1, but the sheath dynamics are mirrored. CCRF discharges with symmetric electrodes exhibit that the sheaths oscillate 180° out of phase at each electrode.

7. Ambipolar field

The temporal dynamics inside the plasma sheaths demonstrate that strong electric fields in the range of several kV/m confine the electrons in the plasma discharge. However, due to the pronounced electron depletion inside the plasma sheaths, no electrons overcome the full sheath potential. Only secondary electrons generated at the electrode would obtain the full voltage drop, which are not included in the present simulation case. Consequently, it is important to pay attention to the ambipolar electric field,[93,95,185] which is much weaker, but many electrons can traverse through this field and gain or lose energy. The ambipolar electric field is quite difficult to detect in Figs. 7(g) and 7(h) (Multimedia view) due to the wide range of values of the electric field strength ($-100 < E < 100$ kV/m). The charge density in Fig. 7(c) (Multimedia view) illustrates an accumulation of electrons at $x \approx 9$ mm and $x \approx 41$ mm, which is pronounced during the fully collapsed sheath, i.e., $0 < t < 35$ ns in front of the

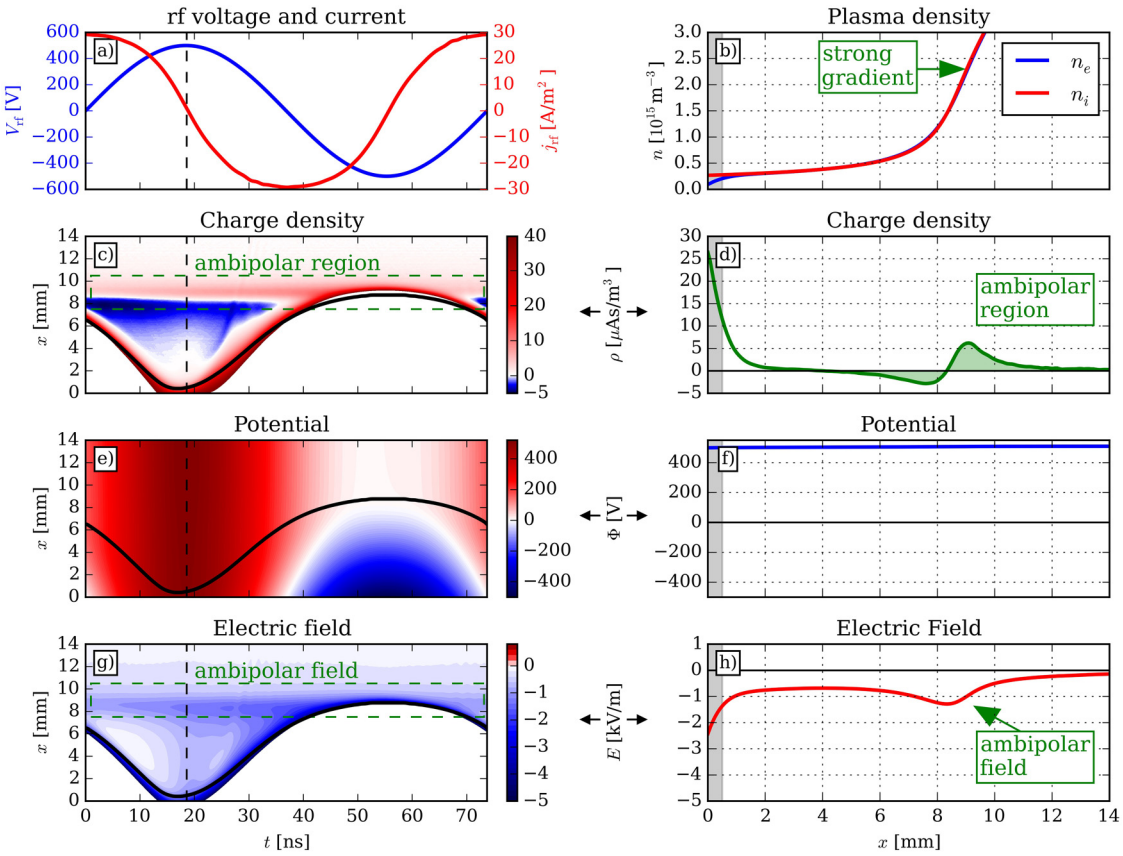

FIG. 9. This is the same plot as Fig. 7 (Multimedia view), but the x axis is adjusted to focus on the region $0 < x < 14$ mm and the scaling of the density, the charge density, and the electric field are adjusted in order to illustrate the dynamics of the ambipolar field. (a) The rf voltage (blue) and the rf current density (red) at the driven electrode, (b) the electron and ion density profile, (c) and (d) the charge density, (e) and (f) the potential, and (g) and (h) the electric field. The left side presents spatio-temporal results, the solid black lines indicate the electron sheath edges, and the vertical black dashed line represents the time that is related to the temporal snapshot on the right side. The gray areas on the right side indicate the plasma sheaths. The color bars indicate the absolute values. Discharge conditions: argon gas, $p = 3$ Pa, $V_0 = 500$ V, $f_{rf} = 13.56$ MHz, $L_{gap} = 50$ mm. The animation available as a supplementary material shows the full dynamics. Multimedia view: https://doi.org/10.1063/5.0003114.2.

sheath at the powered electrode and $35 < t < 70$ ns in front of the sheath at the grounded electrode. This double layer of positive and negative space charges exists, since electrons move away from the ions ($T_e \gg T_i$, $m_e \ll m_i$) in a region of strong density gradients, which is an indication that an electric field arises ($\frac{\partial E}{\partial x} \propto \rho \neq 0$).

Figure 9 (Multimedia view) demonstrates the dynamics of the ambipolar field by zooming into the discharge near the powered electrode ($0 < x < 14$ mm). Additionally, the high electric field strengths are not shown, and the range is set between $-5 < E < 0$ kV/m. The charge density color scale is also adjusted in order to highlight the ambipolar region [green color in Figs. 9(c) and 9(d) (Multimedia view)]. In particular, during the sheath collapse, electrons can react much faster than ions and fill up the depletion zone, which was caused by the fully expanded plasma sheath. However, the ion flux and the electron flux must be coupled locally, and, consequently, an ambipolar field arises in order to draw the electrons back to the ions. Figure 9 (Multimedia view) illustrates the strong density gradient, the ambipolar region, and the ambipolar field (see green markers) at $x \approx 9$ mm. The charge density indicates a double layer structure in this region due to this ambipolar field, and the electric field shows a local extremum. During sheath expansion ($t_2 < t < t_4$), the sheath field increases and couples with the ambipolar field when the sheath is fully expanded. Previous results[93,184] have shown that the ambipolar field in the quasi-neutral plasma bulk can be written as

$$E_{amb}(x, t) = -\frac{T_e}{n_i(x, t)} \frac{\partial n_i(x, t)}{\partial x}. \quad (23)$$

This term is derived from the Boltzmann equilibrium[1,2] under the assumption of a constant electron temperature, and it will play a very important role to understand the complete electron power absorption in Subsection III E.

8. Electron trajectories

Finally, based on the dynamics of the electric field and the densities, electron trajectories are considered in Fig. 10(a) in order to demonstrate the typical behavior of electrons in this regime. The red and the blue dots represent the trajectory of two individual electrons arbitrarily selected in the simulation, respectively. The light red areas represent the plasma sheaths, and the white background illustrates the plasma bulk, which is only shown for orientation. Elastic electron-neutral collisions are depicted by the black circles, and inelastic electron-neutral collisions (excitation and ionization) are depicted by the green circles. Additionally, the corresponding energies of the traced electrons are shown in Fig. 10(b) by the red and blue dashed lines.

In this pressure regime ($p = 3$ Pa), the mean free path of electrons with energies between 10 and 30 eV is $\lambda_m \approx 15$ mm. Scattering events lead to a change in the direction of motion and a redistribution of the velocity components. In the case of an inelastic collision (excitation or ionization), the electron energy changes drastically; e.g., the electron traced by the blue color undergoes an excitation process at $t \approx 39$ ns and loses the energy $\varepsilon_{exc} \approx 11.5$ eV, and the same electron undergoes an ionization process at $t \approx 60$ ns and loses the energy $\varepsilon_{ion} \approx 15.76$ eV. In contrast to the energy loss due to collisions, electrons gain energy during the interaction with the expanding sheath phase; e.g., the electron traced by the blue color penetrates into the sheath at $t \approx 28$ ns with an energy of $\varepsilon \approx 24$ eV and it leaves the sheath with an energy of $\varepsilon \approx 33$ eV. This "kick" of electrons during the sheath expansion leads to an anisotropic energy transfer in the x-direction. These electrons indicate a beam-like behavior before they undergo a collision, and thus, the term electron beam is a proper choice and is used in many studies.[72,73,124,126] The interaction with the plasma sheath during the collapsing phase leads to an energy loss; e.g., the electron traced by the red color loses

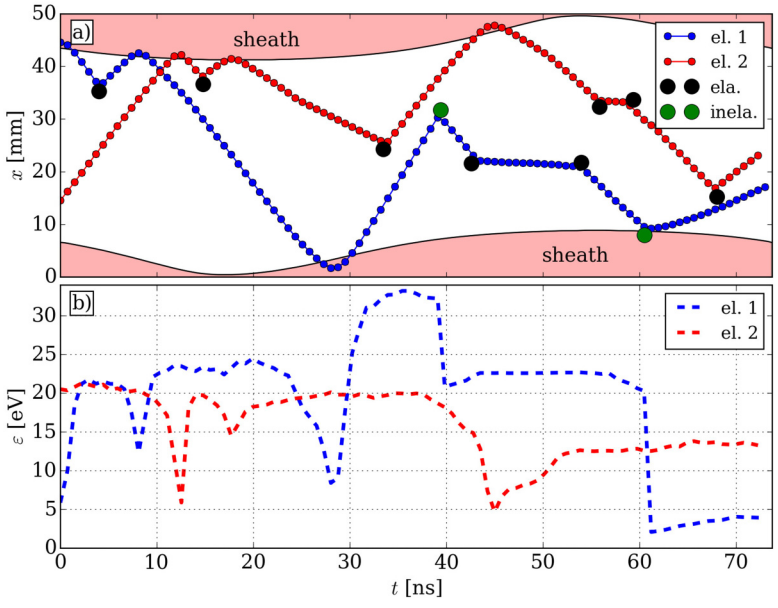

FIG. 10. Two individual electron trajectories marked by the red and blue dots in (a) and the corresponding electron energy in (b) marked by the red and blue dashed lines. The black circles represent elastic electron-neutral collisions, and the green circles represent inelastic electron-neutral collisions (excitation and ionization). The plasma sheaths are marked by the light red areas. Discharge conditions: argon gas, $p = 3$ Pa, $V_0 = 500$ V, $f_{rf} = 13.56$ MHz, $L_{gap} = 50$ mm.

$\Delta\varepsilon \approx 6$ eV at $t \approx 46$ ns. In addition, the ambipolar electric field also contributes to the deceleration and acceleration of electrons in front of the plasma sheath. The electron interaction with the sheath field is traditionally called "collisionless heating," and it is the dominant mechanism of energy transfer to the electrons. These trajectories are for illustration purposes, and the collective behavior must be taken into account to understand the dynamics.

B. Current densities

1. Current conservation

In order to study the collective behavior of the electrons, the current densities are analyzed. At the beginning of Subsection III A in Fig. 7(a) (Multimedia view), the rf current density at the driven electrode was introduced and will be now considered as the total current density $j_{\mathrm{rf}}(t) = j_{\mathrm{tot}}(x, t)$, which flows through the discharge under consideration of current conservation. The total current density is divided into three different current densities,

$$j_{\mathrm{tot}} = j_{\mathrm{i}} + j_{\mathrm{e}} + j_{\mathrm{d}}. \tag{24}$$

Here,

$$j_{\mathrm{e}} = -e\Gamma_{\mathrm{e}} = -en_{\mathrm{e}}u_{\mathrm{e}} \tag{25}$$

and

$$j_{\mathrm{i}} = e\Gamma_{\mathrm{i}} = en_{\mathrm{i}}u_{\mathrm{i}} \tag{26}$$

are the ion $j_{\mathrm{i}} = j_{\mathrm{i}}(x, t)$ and electron $j_{\mathrm{e}} = j_{\mathrm{e}}(x, t)$ current densities. The sum of the ion and electron current densities yields the conduction current density $j_{\mathrm{c}} = j_{\mathrm{c}}(x, t)$;

$$j_{\mathrm{d}} = \epsilon_0 \frac{\partial E}{\partial t} \tag{27}$$

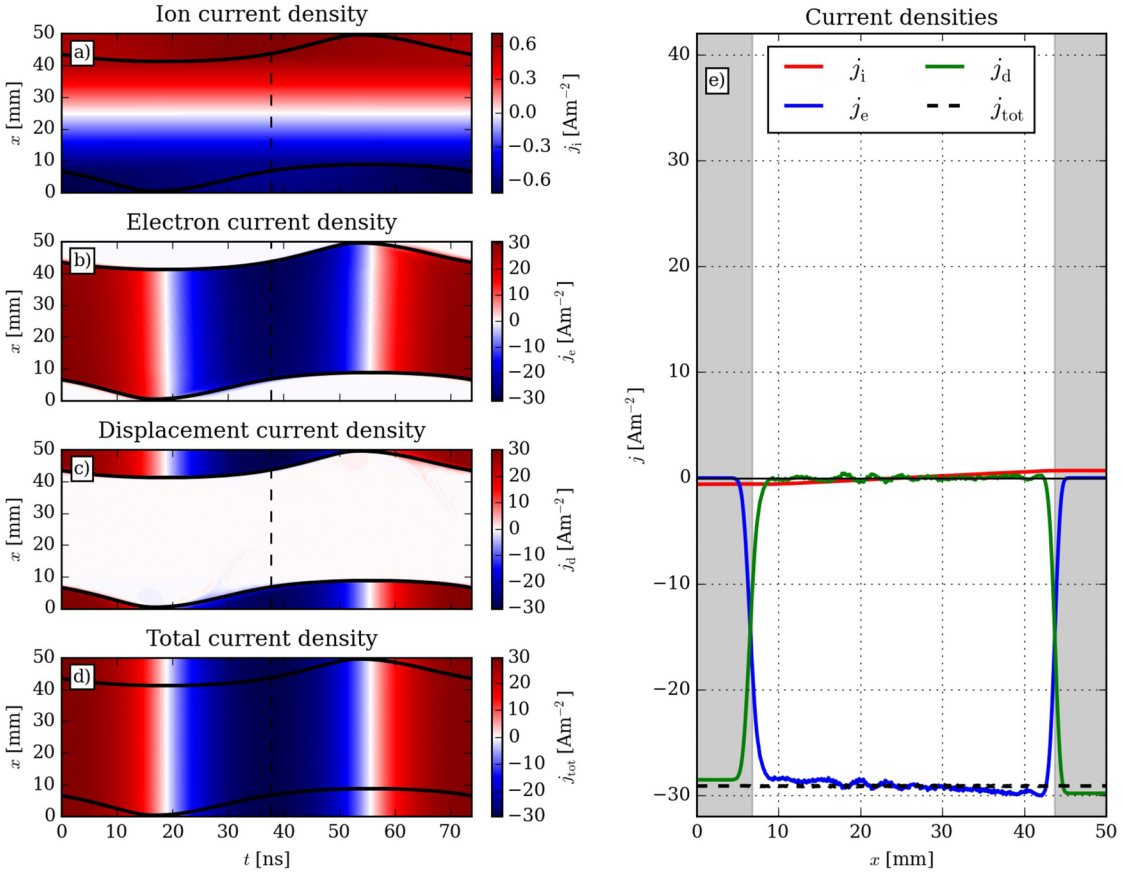

FIG. 11. (a) The ion, (b) electron, (c) displacement, and (d) total current densities. The left side presents spatiotemporal results, the solid black lines indicate the electron sheath edges, and the vertical black dashed line represents the time that is related to the temporal snapshot on the right side in figure (e). The gray areas on the right side indicate the plasma sheaths. The color bars indicate the absolute values. Discharge conditions: argon gas, $p = 3$ Pa, $V_0 = 500$ V, $f_{\mathrm{rf}} = 13.56$ MHz, $L_{\mathrm{gap}} = 50$ mm. The animation available as a supplementary material shows the full dynamics. Multimedia view: https://doi.org/10.1063/5.0003114.3.

is the displacement current density, $j_d = j_d(x, t)$. The current conservation for these current densities must be ensured at all times,

$$\frac{\partial j_{tot}}{\partial x} = \frac{\partial}{\partial x}(\underbrace{j_i + j_e}_{j_c} + j_d) = 0. \tag{28}$$

Current conservation is a different form of Kirchhoff's current law in electrical circuits.

The ion current density is shown in Figs. 11(a) and 11(e) (Multimedia view) by the red solid line. This current density contributes very weakly to the total current density due to the low mean velocity of ions. A slight slope of the ion current density arises from the center to both electrodes due to acceleration by the electric field and the resulting ionization. In contrast, the electron current density [Figs. 11(b) and 11(e), blue solid line (Multimedia view)] dominates in the plasma bulk because of the high electron mean velocity. In the sheath, the electron current density decreases rapidly due to electron depletion. The small slope in the bulk region [see Fig. 11(e), blue solid line (Multimedia view)] correlates with the slope of the ion current density [Fig. 11(e), red solid line (Multimedia view)] in order to fulfill particle flux conservation. The displacement current density [Figs. 11(c) and 11(e), the green solid line (Multimedia view)] indicates the exact opposite trend of the sum of the electron and ion current density, which is physically necessary to ensure current conservation. Therefore, the displacement current density dominates in the sheaths (fast temporal change of the electric field) and is almost zero in the bulk (no significant electric field oscillations). The total current density is presented in Figs. 11(d) and 11(e) (Multimedia view) by the black dashed line. The total current density does not have any spatial modulations in the x-direction; consequently, the black dashed line in Fig. 11(e) (Multimedia view) is constant in space due to current conservation. In addition to these general dynamics, electrostatic wave propagations are visible in the electron (blue line) and in the displacement (green line) current density in Fig. 11(e) (Multimedia view), which are pronounced during sheath expansion. These dynamics can hardly be seen in the spatiotemporal

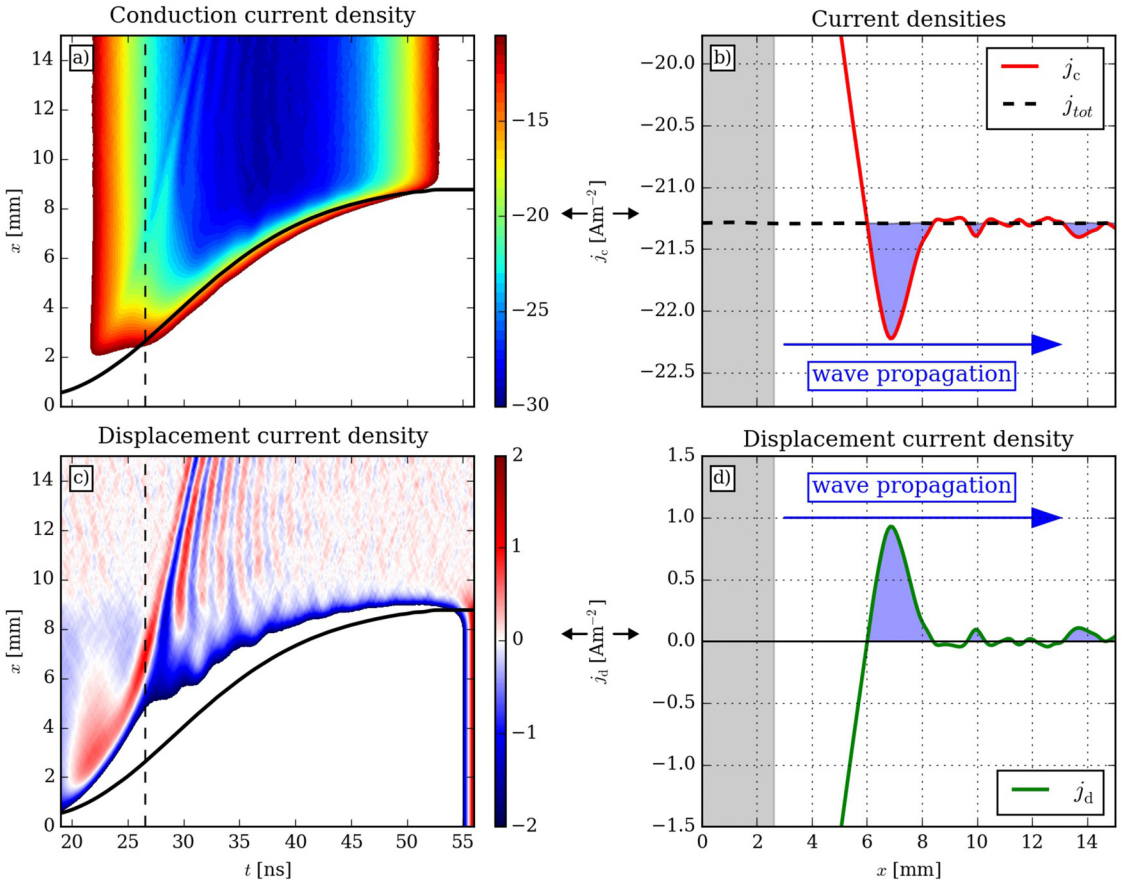

FIG. 12. Conduction (a) and (b) and displacement (c) and (d) current density during sheath expansion at the powered electrode. The color bars indicate the absolute values. Discharge conditions: argon gas, $p = 3$ Pa, $V_0 = 500$ V, $f_{rf} = 13.56$ MHz, $L_{gap} = 50$ mm. The animation available as a supplementary material shows the full dynamics. Multimedia view: https://doi.org/10.1063/5.0003114.4.

plots [Figs. 11(a) and 11(d) (Multimedia view)] due to the color scale. The frequency and the wavelength of the electrostatic waves match the theoretical models[1,4] (dispersion relation of warm electrostatic waves).

2. Electrostatic waves

In order to investigate the origin of these nonlinear waves, the region of interest is focused on the sheath expansion ($20 < t < 55$ ns) adjacent to the plasma sheath at the powered electrode ($0 < x < 15$ mm). The spatiotemporal dynamics of the conduction current density is shown in Fig. 12(a) (Multimedia view) with an adjusted color scale. In Fig. 12(b) (Multimedia view), the spatial dynamics of the conduction current is indicated by the red solid line, and the vertical axis is centered with respect to the total current density (dashed black line). Figures 12(c) and 12(d) (Multimedia view) show the displacement current density. The plots on the right side are snapshots of an animation. The expanding plasma sheath accelerates electrons back into the plasma bulk with higher energies (see the electron trajectory in Fig. 10). Due to the long electron mean free path, the propagation of these beam-like electrons causes a local enhancement of the conduction current density. This local increase [see the blue area in Fig. 12(b) (Multimedia view)] leads to the situation that the conduction current density exceeds the total current density, $|j_c| > |j_{tot}|$. Consequently, the displacement current density [Figs. 11(c) and 11(d), the green solid line (Multimedia view)] has to compensate this local increase and a positive maximum arises. This interplay between the conduction current and the displacement current leads to the generation of electrostatic waves during sheath expansion, which propagate through the plasma bulk. Vender and co-workers[72,107,108] have studied this wave–particle interaction with respect to a pronounced anisotropic distribution function at the electron sheath edge. The frequency of these waves changes during sheath expansion since the plasma density at the electron sheath edge increases, and consequently, the electron plasma frequency becomes higher. Accordingly, electron inertia plays an important role in this nonlinear regime where electrons interact with the plasma sheath. Previous works[72,82,107,109] have also shown that these waves may contribute significantly to the electron power gain and loss dynamics. However, in the presented case, the amplitude of the waves is very small and they do not significantly influence the total current density; i.e., no harmonics in the rf current are visible in Fig. 7(a) (Multimedia view). Section III E will deal with the impact on the total power absorption.

C. Fast and slow electrons

The rapid sheath expansion accelerates electrons into one direction (here, the x-direction) and the collective behavior of these electrons changes from isotropic to anisotropic. The electron energy distribution function (EEDF), f_{EEDF}, in low pressure CCRF discharges typically indicates a non-Maxwellian trend. The integral over all energies of the EEDF yields the electron density,

$$n_e = \int_0^\infty f_{EEDF}(\varepsilon)d\varepsilon. \tag{29}$$

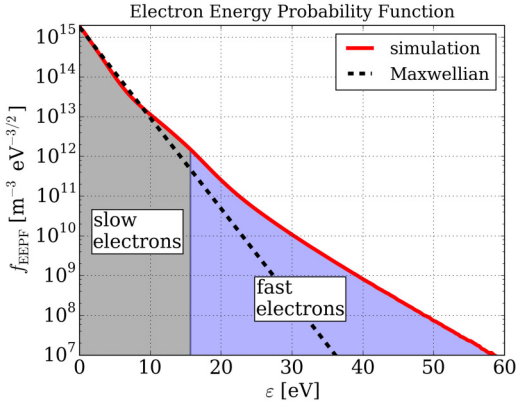

FIG. 13. Spatially and temporally averaged electron energy probability function (red solid line) obtained from the PIC/MCC simulation and a Maxwellian distribution with $T_e = 1.9$ eV (black dashed line). The gray region represents all electrons with energies below 15.7 eV, and the blue region represents all electrons with energies above 15.7 eV, which is the threshold for argon ionization. Discharge conditions: argon gas, $p = 3$ Pa, $V_0 = 500$ V, $f_{rf} = 13.56$ MHz, $L_{gap} = 50$ mm.

Additionally, the averaged energy, $\langle\varepsilon\rangle$, of the electrons is obtained by

$$\langle\varepsilon\rangle = \frac{1}{n_e}\int_0^\infty \varepsilon f_{EEDF}(\varepsilon)d\varepsilon. \tag{30}$$

Frequently, the electron energy probability function (EEPF), f_{EEPF}, is introduced,

$$f_{EEPF} = \frac{f_{EEDF}}{\sqrt{\varepsilon}}. \tag{31}$$

The advantage of the EEPF is that a Maxwellian distribution is a straight line in a semilogarithmic plot, such as shown in Fig. 13. This figure shows the EEPF of the discussed base case (red solid line) averaged over the gap distance and one rf cycle. The black dashed line in Fig. 13 indicates a Maxwellian distribution with an electron temperature of $T_e = 1.9$ eV. This value is calculated from the simulation by using the thermodynamic relation with respect to the averaged energy,

$$\langle\varepsilon\rangle = \frac{3}{2}T_e. \tag{32}$$

The difference between the solid red and the dashed black line clearly illustrates the critical approach of a thermodynamic relation. Additionally, the EEPF is also a function of time and space, and thus, the difference would be more extreme, especially at the position of the electron sheath edge during sheath expansion.[72] The classical terminology of the electron temperature in combination with a Maxwell distribution might be a good approximation for the low energy electrons, but particularly for the high energy electrons ($\varepsilon > 15$ eV),

strong differences are demonstrated. In Subsection III D, the concept of a kinetic electron temperature will be presented. A general idea of considering any kind of distribution function is to split the electrons into two different energy groups, which are called the following: slow electrons with energies below 15.7 eV, marked by the gray region in Fig. 13, and fast electrons with energies above 15.7 eV, marked by the blue region in Fig. 13. The chosen energy is not related to the trend of the distribution function, but it is the first ionization energy of argon, which is the most important ionization channel to sustain the plasma under the conditions discussed in this tutorial. At higher pressures and/or in magnetized plasmas, other ionization mechanisms such as pooling[186,187] and stepwise[188] ionization can also play an important role. Based on this idea, the dynamics of these different energy groups as well as the excitation and ionization processes are illustrated in Fig. 14, and the full dynamics are shown in the animation. Figures 14(a) and 14(b) (Multimedia view) indicate the density of slow electrons. No specific dynamics are shown except the electron density modulation in the sheath regions. Particularly, Fig. 14(b) (Multimedia view) shows the same profile and the same magnitudes compared to Fig. 7(b) (Multimedia view) where all electrons are considered. This is because electrons with energies between 0 and 15.7 eV usually represent more than 99% of the population of all electrons in such discharges. Figures 14(c) and 14(d) (Multimedia view) show the dynamics of fast electrons with energies above 15.7 eV, and the density is more than two magnitudes lower compared to the density of slow electrons. However, only these electrons can ionize the background gas and also contribute significantly to the excitation process (threshold for argon excitation is 11.5 eV). Consequently, the ionization rate [see Figs. 14(e) and 14(f) (Multimedia view)] and the excitation rate [see Figs. 14(g) and 14(h) (Multimedia view)] indicate the same dynamics compared to that of the fast electrons. Particularly, the excitation rate can be linked to the optical emission and measured experimentally by phase resolved optical emission spectroscopy, and previous work has shown that the dynamics look similar to simulation results.[94,128,130] However, the

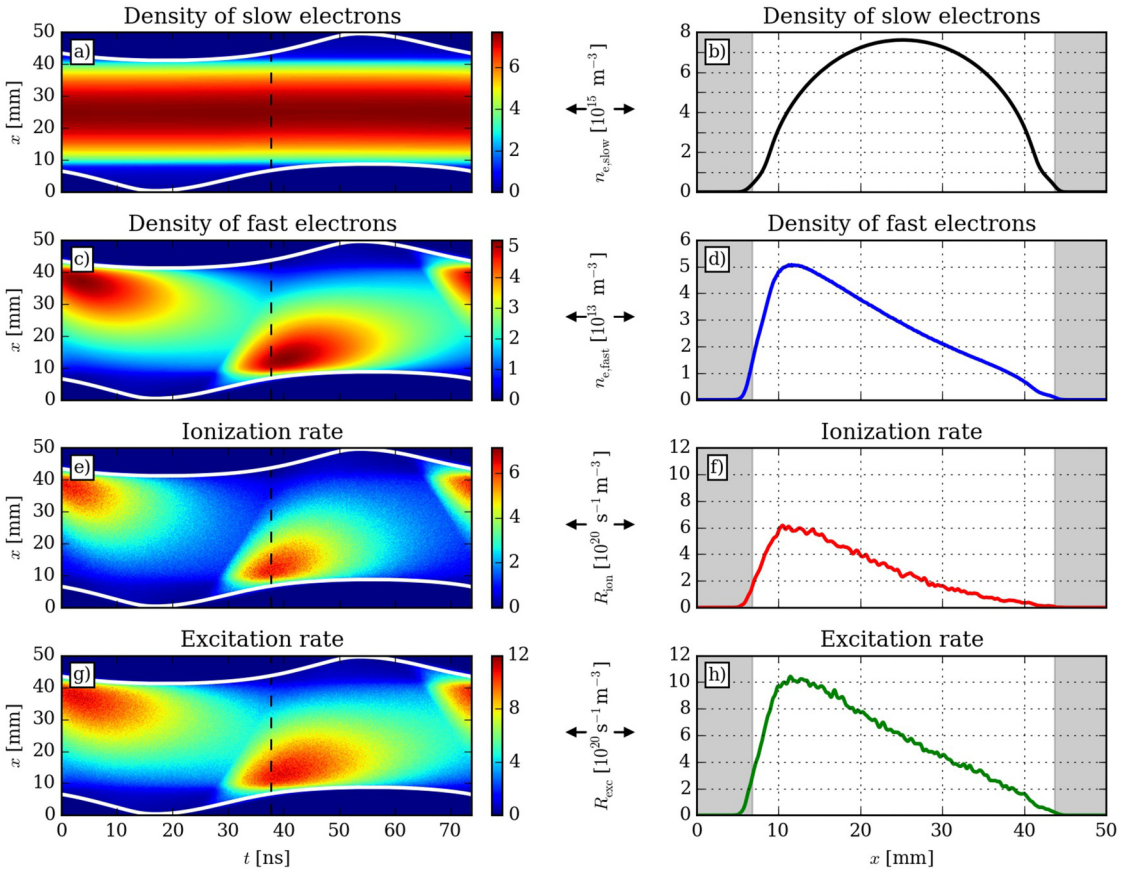

FIG. 14. The density of electrons with energies below 15.7 eV [(a) and (b)] and with energies above 15.7 eV [(c) and (d)], the ionization rate [(e) and (f)], and the excitation rate [(g) and (h)]. The left side presents spatiotemporal results, the solid white lines indicate the electron sheath edges, and the vertical black dashed line represents the time that is related to the temporal snapshot on the right side. The gray areas on the right side indicate the plasma sheaths. The color bars indicate the absolute values. Discharge conditions: argon gas, $p = 3$ Pa, $V_0 = 500$ V, $f_{rf} = 13.56$ MHz, $L_{gap} = 50$ mm. The animation available as a supplementary material shows the full dynamics. Multimedia view: https://doi.org/10.1063/5.0003114.5.

ionization process is more relevant in order to control the plasma with respect to the plasma density. The density of these fast electrons increases substantially during sheath expansion, where electrons are reflected back into the bulk with higher energies due to the strong increase of the electric field in the plasma sheath. Because of the low pressure ($p = 3$ Pa), most of the fast electrons can penetrate a few mm into the plasma bulk without any collisions. In Fig. 10(a), the blue trajectory indicates a typical electron that contributes to the density of fast electrons. Recent work[124,125,127–130] interprets the emphasized red structure in Figs. 14(c), 14(e), and 14(g) (Multimedia view) during sheath expansion as a beam of energetic electrons. However, this term is sometimes misleading without the correct definition. As mentioned before, during the phase of sheath expansion, electrons are reflected back with higher energies due to an increase of the v_x velocity. Consequently, the collective electron motion becomes more anisotropic, but the magnitude of the perpendicular velocity component is still unchanged after the sheath interaction and before the next collision. Due to the relatively long electron mean free path in this pressure regime, the reflected electrons penetrate into the bulk with a beam-like behavior and they lose this dynamics only after undergoing collisions. Additionally, it is important to note that this beam of electrons is not monoenergetic; instead, it is a distribution of electrons with different energies propagating through the plasma bulk. The dynamics and the distribution of these electron beams strongly depend on the dynamics of the plasma sheath and the electron mean free path, e.g., the velocity of the electron sheath edge during expansion and the electric field strength in the sheath. Different experimental studies as well as simulation work have shown that changing basic discharge parameters, such as the gap size, the driving frequency, and the voltage waveform, provide the opportunity to control the dynamics of these electron beams.[97,129]

D. Electron temperature

One of the most important questions in technological low pressure radio frequency discharges is how do electrons gain and lose their energy? The traditional terminology of this mechanism is called electron heating; however, this term might be sometimes misleading because the term 'heating" originates from the field of thermodynamics and is related to an increase of the temperature. In Subsection III C, the EEPF in Fig. 13 has clearly shown that a unique electron temperature based on a Maxwellian distribution is only a good approximation for the low energetic electrons.

In order to discuss how electrons gain and lose their energy, the term electron power absorption is more appropriate and can be studied by the electron power density, $P_e = P_e(x, t)$, which is the product of the electric field and the electron current density,

$$P_e = j_e \cdot E. \tag{33}$$

Figures 15(a) and 15(b) (Multimedia view) show the electron power density. The dominant phase where electrons gain their energy (red color) is during sheath expansion. In contrast, during the collapsing phase, electrons lose their energy (blue color). The animation corresponding to Fig. 15(b) indicates that two pronounced peaks arise, during both, the collapsing and expanding phase. One peak is related to the electron power gain and loss in the plasma sheath due to the electric field, and the second peak is generated due to the ambipolar electric field in front of the plasma sheath. At the maximum sheath expansion, these peaks merge together. The different ways of electron power gain and loss are discussed in Subsection III E. This electron power absorption shall now be linked to the electron temperature. A kinetic concept of the electron temperature is introduced based on the parallel and perpendicular pressure, defined in Eqs. (11) and (12). The parallel, $T_\parallel = T_\parallel(x, t)$, and perpendicular, $T_\perp = T_\perp(x, t)$, electron temperature are obtained by dividing Eqs. (11) and (12) by the electron density,

$$T_\parallel = m_e\left(\langle v_\parallel^2\rangle - u_e^2\right), \tag{34}$$

$$T_\perp = \frac{1}{2} m_e \langle v_\perp^2\rangle. \tag{35}$$

Figures 15(c) and 15(d) (Multimedia view) present the parallel temperature, and Figs. 15(e) and 15(f) (Multimedia view) show the perpendicular temperature. Figures 15(g) and 15(h) (Multimedia view) display the difference between the parallel and the perpendicular temperature $T_\parallel - T_\perp$. If the difference is zero, the temperature elements are equal and the electron distribution is isotropic at this position and time. In the center of the discharge ($x = 25$ mm), the parallel and perpendicular temperature are approximately equal ($T_\parallel \approx T_\perp \approx 1.9$ eV) during the full rf cycle. This value is in good agreement with the temperature calculated by the thermodynamic relation [Eq. (32)], which was discussed in Sec. III C. This is because most of the energetic beam electrons that are responsible for the anisotropy do not reach the center of the discharge without any collisions. However, the anisotropy of the temperature, i.e., the strong difference in $T_\parallel - T_\perp$ [see Figs. 15(g) and 15(h) (Multimedia view)], increases from the center of the discharge to the electrodes. It is important to note that in the plasma sheath, the depicted temperatures show a lot of noise. This is due to electron depletion inside the plasma sheath, and therefore, the results of the temperature very close to the electrode are imprecise. The most significant difference between the parallel and the perpendicular temperature is found during sheath expansion, e.g., $t \approx 30$ ns and $x \approx 8$ mm, where most of the energetic beam electrons are generated. During this phase, the parallel temperature reaches a maximum of $T_\parallel \approx 4$ eV. On the other hand, during the collapsing sheath phase, a minimum of $T_\parallel \approx 1.7$ eV arises due to deceleration of electrons. Normally, the parallel electric field would only affect the parallel temperature $T_\parallel$; however, due to collision events, the perpendicular temperature, $T_\perp$, is also influenced near the plasma sheath. Consequently, the perpendicular temperature, $T_\perp$, temporally lags behind the parallel temperature $T_\parallel$. This means that electrons gain energy during sheath expansion, but they need a certain time to redistribute the energy into the perpendicular components. This concept is a more reasonable method to calculate the electron temperature compared to the thermodynamic relation because the anisotropy (disparity between the parallel and perpendicular temperature) as well as the spatiotemporal dynamics are reflected well. The dynamics of the electron power density and the electron temperature show a similar trend; however, differences are present

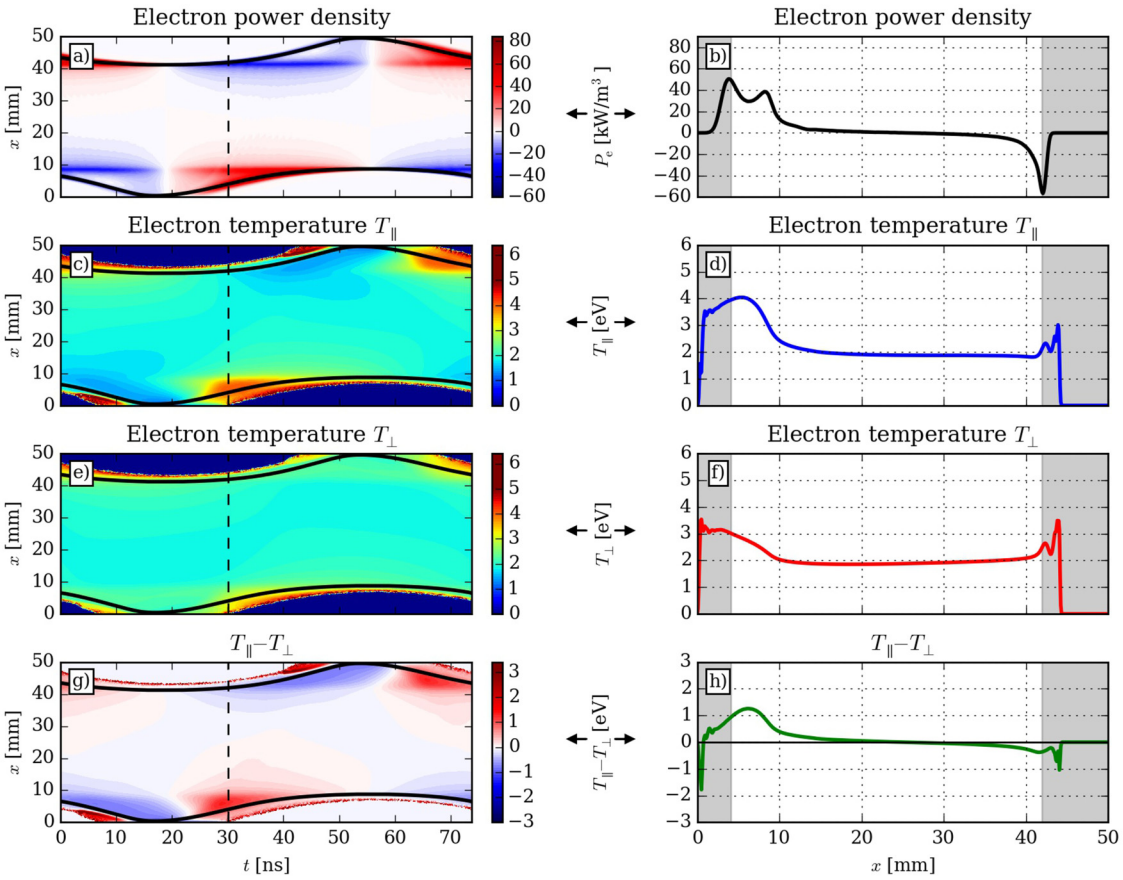

FIG. 15. Electron power density [(a) and (b)], the parallel temperature $T_\parallel$ [(c) and (d)], the perpendicular temperature $T_\perp$ [(e) and (f)], and the difference between both temperatures $T_\parallel - T_\perp$ [(g) and (h)]. The left side presents spatiotemporal results, the solid black lines indicate the position of the sheath, and the vertical black dashed line represents the time that is related to the temporal snapshot on the right side. The gray areas on the right side indicate the plasma sheaths. The color bars indicate the absolute values. Discharge conditions: argon gas, $p = 3$ Pa, $V_0 = 500$ V, $f_{rf} = 13.56$ MHz, $L_{gap} = 50$ mm. The animation available as a supplementary material shows the full dynamics. Multimedia view: https://doi.org/10.1063/5.0003114.6.

($P_e \sim T_\parallel$) because the physical concept of electron power absorption and the temporal change of the electron temperature is different. The electron power absorption shows how electrons gain and lose their energy according to the interaction with the electric fields, which will be clarified in detail in Subsection III E. The parallel and perpendicular temperature are energy reservoirs and store the energy. Therefore, these two terms contribute to the electron energy density, w, which occurs in the energy balance equation (38),

$$w = \frac{1}{2} n_e \left(m_e u_e^2 + T_\parallel + 2T_\perp \right). \tag{36}$$

E. Mechanisms of electron power absorption

In Subsection III D, the electron power absorption was introduced, and the differences of the kinetic electron temperature components were illustrated. The electron power absorption clearly shows when and where electrons gain and lose their energy. During the past few decades, several concepts of electron power absorption ("electron heating") in CCRF discharges have been introduced as well as different modes of discharge operations. In this subsection, a consistent and complete description of the electron power absorption is presented by analyzing the moments of the Boltzmann equation with respect to the parallel direction, x.

In Sec. II, moments of the Boltzmann equations were introduced. Every individual term of the resulting conservation equations (13)–(15) can be computed by the PIC/MCC simulation. In order to study the electron power absorption in detail, the momentum balance Eq. (14) can be rearranged by solving it for the electric field,

$$E = \underbrace{-\frac{m_e}{n_e}\left(\frac{\partial(u_e n_e)}{\partial t} + \frac{\partial(n_e u_e^2)}{\partial x}\right)}_{E_{in}} \underbrace{-\frac{1}{e n_e}\frac{\partial p_{xx}}{\partial x}}_{E_{pr}} \underbrace{-\frac{1}{n_e e}\Pi_c}_{E_{Ohm}}. \tag{37}$$

On the right hand side, three different electric field terms are introduced: the electric field based on inertial effects, E_{in}; the electric field related to the pressure gradient, E_{pr}; and the electric field due to collisions, also called the Ohmic field, E_{Ohm}. Multiplying Eq. (37) by the electron current density, j_e, an equation for the electron power absorption, $P_e(x, t)$, is obtained,

$$\underbrace{j_e E}_{P_e} = \underbrace{\underbrace{j_e E_{in}}_{P_{in}} + \underbrace{j_e E_{pr}}_{P_{pr}}}_{P_{collisionless}} + \underbrace{\underbrace{j_e E_{Ohm}}_{P_{Ohm}}}_{P_{collisional}}. \quad (38)$$

This concept has been introduced in previous works.[75,76,185,189] Figure 16 (Multimedia view) presents the dynamics of the total electron power density, P_e [Figs. 16(a) and 16(e), black dashed line]; the power density due to inertial effects, P_{in} [Figs. 16(b) and 16(e), green solid line]; the power density due to pressure effects, P_{pr} [Figs. 16(c) and 16(e), red solid line]; and the Ohmic electron power density, P_{Ohm} [Figs. 16(d) and 16(e), blue solid line]. Next, the individual terms are explained, and their impact on the total power electron density is analyzed.

1. Inertia power absorption

The first term is the electron power absorption due to electron inertia, $P_{in}(x, t)$, and it is assigned to a collisionless phenomenon. The first part of this term is proportional to the time derivative of the electron flux density, $\frac{\partial \Gamma_e}{\partial t}$, and the second part is proportional to the gradient of the product of the electron flux times the electron mean velocity, $\frac{\partial(\Gamma_e u_e)}{\partial x}$. The dynamics of the electron flux were discussed in subsection III B with respect to the electron current density ($j_e = -e\Gamma_e$). The temporal and spatial dynamics in Fig. 11(e) (Multimedia view) explain the behavior of the inertial term, P_{in}. The electrostatic waves, which were observed in the electron and

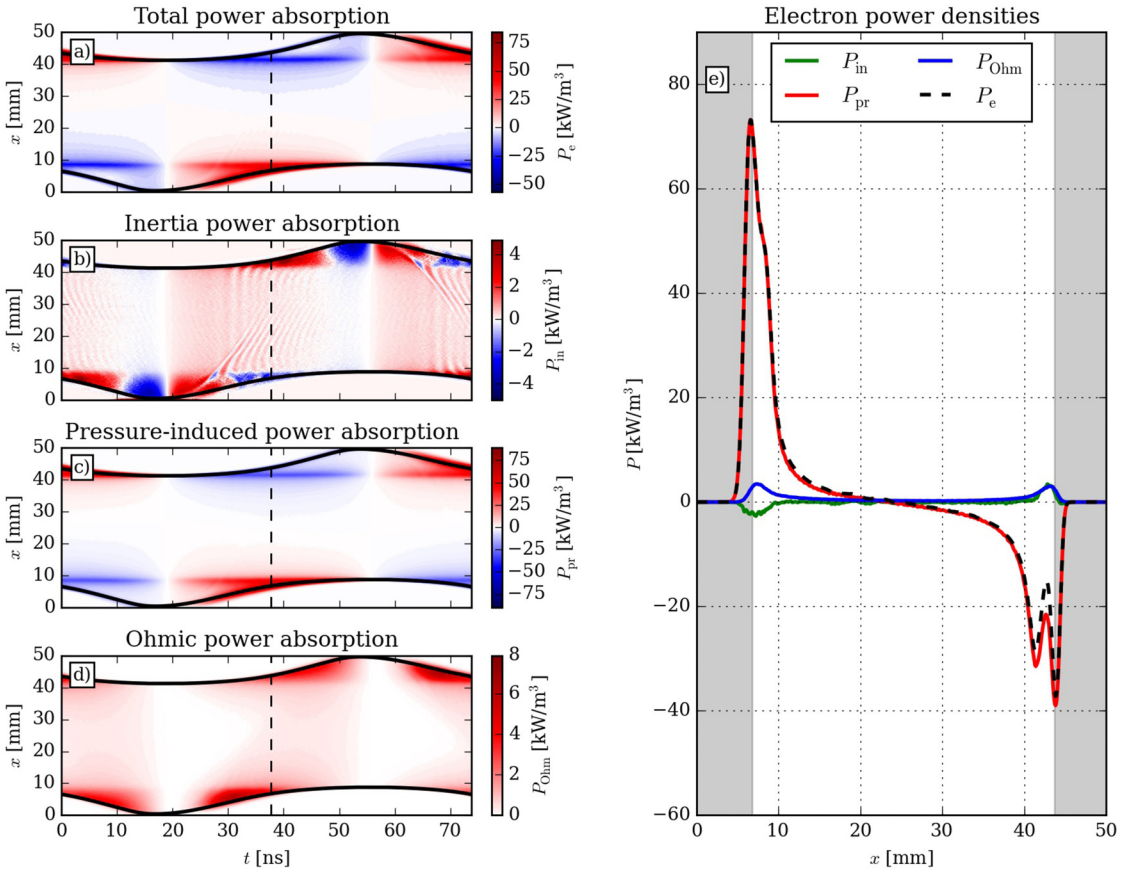

FIG. 16. (a) Electron power density, P_e; (b) electron power absorption due to inertia effects, P_{in}; (c) electron power absorption due to pressure heating, P_{pr}; and (d) electron power absorption due to collisional dynamics, P_{Ohm}. The left side presents spatiotemporal results, the solid black lines indicate the positions of the electron sheath edges, and the vertical black dashed line represents the time that is related to the temporal snapshot on the right side. The gray areas on the right side indicate the sheaths. The color bars indicate the absolute values. Discharge conditions: argon gas, $p = 3$ Pa, $V_0 = 500$ V, $f_{rf} = 13.56$ MHz, $L_{gap} = 50$ mm. The animation available as a supplementary material shows the full dynamics. Multimedia view: https://doi.org/10.1063/5.0003114.7.

displacement current density in the plasma bulk, are also visible in the electron power density in Fig. 16(b) (Multimedia view) (a fine pattern with a slope). In addition to these waves, very weak plasma oscillations are also present. Both the wave propagation as well as the plasma oscillations lead to temporal change of the local electron flux. According to Eqs. (37) and (38), this temporal change leads to a contribution to the electron power absorption based on inertial effects, since oscillations as well as waves have their origin in the electron plasma frequency which represents the inertia. The contribution in the plasma bulk to the total electron power density is less than 1 kW/m^3, and thus, only a fraction is almost negligible. In addition to the temporal change of the electron flux, significant gradients are also present in the electron current density in Fig. 11(e) (Multimedia view). In particular, at the transition between the plasma bulk and the sheath, the electron current density changes abruptly due to the electron depletion inside the sheath. Therefore, an electron power gain region occurs [a dark red structure in Fig. 16(b) (Multimedia view)] close to the electron sheath edge during the collapsing and expanding phase of the electron sheath edge. During the full sheath collapse, a negative electron power density occurs. These power gain and loss dynamics reach values up to $\pm$ 4 W/m^3, which is still low compared to the total electron power density. The spatially and temporally averaged power density is $\langle P_{\mathrm{in}}\rangle_{x,t} \approx 0.75$ W/m^3. In comparison with the total electron power density, $\langle P_{\mathrm{e}}\rangle_{x,t} \approx 1275$ W/m^3, it is only 0.1%. Finally, for this particular case, P_{in} does not play an important role, since the waves and oscillations are only weakly excited. Nevertheless, this contribution may become important in a regime where the excitation of the plasma series resonance as well as plasma waves plays a more relevant role.

2. Pressure-induced power absorption

The second term, $P_{\mathrm{pr}}(x, t)$, in Eq. (38) represents the electron power absorption due to pressure effects and is also a collisionless mechanism. In general, this term is strongly related to the classical concept of "pressure heating," which was developed by Turner and co-workers[90–92] It is more appropriate to divide this term into two parts using the product rule,

$$P_{\mathrm{pr}} = j_{\mathrm{e}} \underbrace{\frac{1}{e n_{\mathrm{e}}} T_{\parallel} \frac{\partial n_{\mathrm{e}}}{\partial x}}_{E_{\nabla n_{\mathrm{e}}}} + j_{\mathrm{e}} \underbrace{\frac{1}{e} \frac{\partial T_{\parallel}}{\partial x}}_{E_{\nabla T}}. \tag{39}$$

The first term includes an electric field, $E_{\nabla n_{\mathrm{e}}}$, which looks very similar compared to the ambipolar electric field, E_{amb}, which was introduced in Eq. (23) of Subsection III A. The difference is that the ion density is replaced by the electron density, and the electron temperature is a function of space and time. The second term depends on the gradient of the parallel temperature whose dynamics were discussed in Subsection III D in Figs. 15(c) and 15(d) (Multimedia view). The values in Fig. 16(c) (Multimedia view) and the red solid line in Fig. 16(e) (Multimedia view) indicate that P_{pr} is the dominant power absorption mechanism. The ambipolar electric field makes a significant contribution, and the horizontal ambipolar region in front of the electron sheath edge [see Fig. 9 (Multimedia view)] is well depicted in Fig. 16(c) (Multimedia view). The details of the interplay between the electron density gradient and the gradient of the parallel temperature are not discussed in this work but can be found in previous work.[185] It is important to note that the electron power gain and loss dynamics of the term P_{pr} do not balance; i.e., the absolute value of the negative part [blue color in Fig. 16(c) (Multimedia view)] of P_{pr} is significantly smaller than the positive part [red color in Fig. 16(c) (Multimedia view)]. This is because of the temporal asymmetry of the parallel temperature that contributes to the ambipolar field. Figures 15(c) and 15(d) (Multimedia view) indicate that during sheath expansion, the electron temperature increases more drastically compared to the time during sheath collapse. Consequently, the electron power gain due to pressure effects must be higher during sheath expansion. In total, the temporally and spatially averaged value of the electron power absorption due to pressure effects is $\langle P_{\mathrm{pr}}\rangle_{x,t} \approx 807$ W/m^3, which is approximately 63% of the total electron power density.

3. Ohmic power absorption

The last term in Eq. (38) is the electron power absorption due to collisions, P_{Ohm}, henceforth termed Ohmic power absorption. This term is different from the classical definition of "Ohmic heating,"[1–3] which is calculated by the momentum balance equation, neglecting all spatial derivatives, assuming a harmonic time dependence of the electric field and using a simplified version of the collisional electron momentum loss. In this analysis, the change of momentum due to collisions is computed in the PIC/MCC simulations from the accumulated change of the x components of the velocities of super particles undergoing collisions. A detailed description and calculation of this term can be found in the previous work.[76]

Figure 17 shows the collisional electron momentum loss. Most of the momentum loss occurs very close to sheath expansion because this is the region of an electron population with a high parallel velocity component (pronounced anisotropy). Consequently, the Ohmic power absorption increases in this region. Figure 16(d) (Multimedia view) and the blue solid line in Fig. 16(e) (Multimedia view) show the dynamics of the Ohmic power absorption and clearly demonstrate a maximum of P_{Ohm} in front of the electron sheath

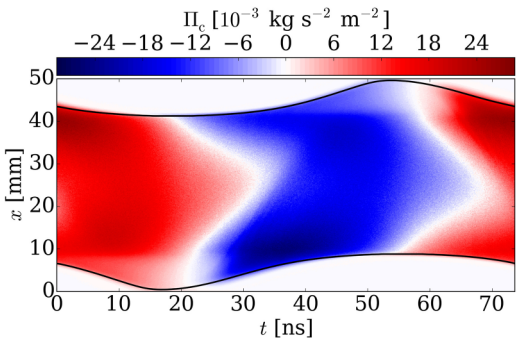

FIG. 17. The spatial and temporal dynamics of the collisional electron momentum loss, Π_{c}. The black solid lines represent the electron sheath edges. Discharge conditions: argon gas, $p = 3$ Pa, $V_0 = 500$ V, $f_{\mathrm{rf}} = 13.56$ MHz, $L_{\mathrm{gap}} = 50$ mm.

edge. The Ohmic power absorption is always positive, and the temporal and spatial averaged value is $\langle P_{\mathrm{Ohm}} \rangle_{x,t} \approx 468\ \mathrm{W/m^3}$, which is approximately 37 % of the total electron power absorption.

4. Conclusion: Power absorption analysis

This power absorption analysis is fully self-consistent and clearly distinguishes between collisionless and collisional power absorption. In the presented case, the electron power absorption due to pressure effects dominates, followed by the Ohmic power absorption, and the power absorption due to inertial effects is only in the range of 0.1%. However, it should be kept in mind that the contribution of the different power absorption mechanisms strongly depends on the discharge conditions.

IV. CONCLUSION

A. Summary

Low pressure capacitively coupled radio frequency discharges exhibit quite complex particle–field and particle–particle interaction. Due to the long mean free path, nonlocal and nonlinear dynamics play a crucial role and change the electron distribution function in an anisotropic manner. Particle-in-cell/Monte Carlo collision simulations capture all these effects. Using the appropriate diagnostics in the simulation, the details of the electron dynamics can be understood on a nanosecond timescale. This tutorial has shown as to how the electric field influences the particle dynamics. The collapsing sheath phase leads to deceleration of electrons and the expanding sheath phase to acceleration of electrons along the axial direction. In addition, the ambipolar electric field in front of the electron sheath edges plays a pivotal role in the coupling power to the electrons. During sheath expansion, the acceleration of beam-like electrons causes a local enhancement of the conduction current, which has to be compensated by the local displacement current in order to ensure current continuity. The interplay between these two current densities adjacent to the nonlinear plasma sheath leads to the excitation of electrostatic waves that propagate into the plasma bulk.

The electron beams that are generated during sheath expansion penetrate into the plasma bulk almost collisionlessly and cause an anisotropy in the distribution function, which cannot be explained by the drift-diffusion theory. The dynamics of these energetic electron beams are well represented by taking into account the density of electrons with energies above 15.7 eV. A pronounced maximum of the density of fast electrons arises during sheath expansion, which creates peaks in the spatiotemporal distribution of the excitation and ionization rate. Due to the anisotropy, a unique electron temperature cannot be determined according to the thermodynamic relation. However, a kinetic temperature was introduced, which can be divided into the parallel temperature (orientation of the electric field) and the perpendicular temperature. These distinct temperatures were computed in the PIC/MCC simulations. The parallel temperature was found to increase during sheath expansion, and due to collisions, the perpendicular temperature lags behind but also increases. This temperature increase allows for an unambiguous definition of heating, since the collisions redistribute the velocity components, and, consequently, in the center of the discharge, the distribution function indicates an isotropic behavior.

The question as to how electrons gain and lose their energy was answered by studying the terms of the electron momentum balance equation. This analysis clearly showed how the collisional and collisionless power absorption really works. It was found that most of the electrons gain their energy collisionlessly due to pressure-induced effects (63%, for the case analyzed) during the time of sheath expansion and in the ambipolar field region in front of the electron sheath edge. Collisional (Ohmic) power absorption also occurs in the vicinity of the sheath during expansion and indicated a moderate contribution of 37% to the total power absorption. Overall, it was shown how the individual parameters (densities, fluxes, temperatures, and power densities) are related and how the electron dynamics can be investigated in detail on the basis of a self-consistent kinetic particle simulation.

B. Outlook

The concept of this tutorial is basically suitable for any kind of CCRF discharge, which can be investigated by means of 1d3v PIC/MCC simulations. Changing parameters, such as the pressure, the rf voltage amplitude, the radio frequency, and the gap distance will show more or different features about the electron dynamics. Adding more complex chemistry, such as that typical for electronegative gases,[44,94] will also yield different results, which might be more relevant for industrial applications. Furthermore, plasma-surface interactions[54,104] have to be taken into account since secondary electrons can obtain the full sheath potential and contribute to the nonlocal and nonlinear electron dynamics. Many CCRF discharges are geometrically asymmetric (different electrode areas of the grounded and powered electrode); hence, 2D simulations or at least a 1D cylindrical[82,190] setup are necessary in order to investigate the influence of a DC self-bias. The impact of different voltage waveforms has to be investigated, such as dual-[111,112,191] or multi-frequency[13,192,193] discharges or saw-tooth[130] waveforms. Particularly, the calculation of the moments of the distribution function by means of PIC/MCC simulations may build a bridge between particle based and fluid simulations in order to demonstrate the limitations of fluid models in the low pressure regime.

ACKNOWLEDGMENTS

This work was funded by the German Research Foundation (DFG) in the frame of the project "Electron heating in capacitive RF plasmas based on moments of the Boltzmann equation: from fundamental understanding to knowledge based process control" (No. 428942393). Support by the DFG via SFB TR 87 (No. 138690629), projects C1 and C8, SFB 1316 (No. 327886311), project A4, DFG project (No. MU 2332/6-1) and by the Hungarian Office for Research, Development, and Innovation (No. NKFIH 119357) is gratefully acknowledged.

REFERENCES

[1]M. A. Lieberman and A. J. Lichtenberg, *Principles of Plasma Discharges and Materials Processing* (John Wiley & Sons, 2005).
[2]P. Chabert and N. Braithwaite, *Physics of Radio-frequency Plasmas* (Cambridge University Press, 2011).

[3]Y. P. Raizer, M. N. Shneider, and N. A. Yatsenko, *Radio-frequency Capacitive Discharges* (CRC Press, 2017).
[4]F. F. Chen, *Introduction to Plasma Physics* (Springer Science & Business Media, 2012).
[5]T. Makabe and Z. L. Petrovic, *Plasma Electronics: Applications in Microelectronic Device Fabrication* (CRC Press, 2014).
[6]D. B. Graves, "Plasma processing," IEEE Trans. Plasma Sci. **22**, 31–42 (1994).
[7]M. Sekine, "Dielectric film etching in semiconductor device manufacturing: Development of SiO_2 etching and the next generation plasma reactor," Appl. Surf. Sci. **192**, 270–298 (2002).
[8]S. Samukawa, M. Hori, S. Rauf, K. Tachibana, P. Bruggeman, G. Kroesen, J. C. Whitehead, A. B. Murphy, A. F. Gutsol, S. Starikovskaia *et al.*, "The 2012 plasma roadmap," J. Phys. D: Appl. Phys. **45**, 253001 (2012).
[9]I. Adamovich, S. D. Baalrud, A. Bogaerts, P. Bruggeman, M. Cappelli, V. Colombo, U. Czarnetzki, U. Ebert, J. G. Eden, P. Favia *et al.*, "The 2017 plasma roadmap: Low temperature plasma science and technology," J. Phys. D: Appl. Phys. **50**, 323001 (2017).
[10]B. Radjenović and M. Radmilović-Radjenović, "The implementation of the surface charging effects in three-dimensional simulations of SiO_2 etching profile evolution," Engineering **6**, 1 (2014).
[11]H. Jansen, M. de Boer, R. Wiegerink, N. Tas, E. Smulders, C. Neagu, and M. Elwenspoek, "RIE lag in high aspect ratio trench etching of silicon," Microelectron. Eng. **35**, 45–50 (1997).
[12]J. Arnold and H. H. Sawin, "Charging of pattern features during plasma etching," J. Appl. Phys. **70**, 5314–5317 (1991).
[13]F. Krüger, S. Wilczek, T. Mussenbrock, and J. Schulze, "Voltage waveform tailoring in radio frequency plasmas for surface charge neutralization inside etch trenches," Plasma Sources Sci. Technol. **28**, 075017 (2019).
[14]N. Chekurov, K. Grigoras, A. Peltonen, S. Franssila, and I. Tittonen, "The fabrication of silicon nanostructures by local gallium implantation and cryogenic deep reactive ion etching," Nanotechnology **20**, 065307 (2009).
[15]J. Park, N.-E. Lee, J. Lee, J. Park, and H. Park, "Deep dry etching of borosilicate glass using SF_6 and SF_6/Ar inductively coupled plasmas," Microelectron. Eng. **82**, 119–128 (2005).
[16]S. Kong, K. Minami, and M. Esashi, "Fabrication of reactive ion etching systems for deep silicon machining," IEEJ Trans. Sens. Micromachines **117**, 10–14 (1996).
[17]H. V. Jansen, M. J. de Boer, S. Unnikrishnan, M. Louwerse, and M. C. Elwenspoek, "Black silicon method X: A review on high speed and selective plasma etching of silicon with profile control: An in-depth comparison between Bosch and cryostat DRIE processes as a roadmap to next generation equipment," J. Micromech. Microeng. **19**, 033001 (2009).
[18]F. Laermer, S. Franssila, L. Sainiemi, and K. Kolari, "Deep reactive ion etching," in *Handbook of Silicon Based MEMS Materials and Technologies* (Elsevier, 2015), pp. 444–469.
[19]A. W. Topol, D. La Tulipe, L. Shi, D. J. Frank, K. Bernstein, S. E. Steen, A. Kumar, G. U. Singco, A. M. Young, K. W. Guarini *et al.*, "Three-dimensional integrated circuits," IBM J. Res. Develop. **50**, 491–506 (2006).
[20]J. Trieschmann, F. Schmidt, and T. Mussenbrock, "Particle-in-cell/test-particle simulations of technological plasmas: Sputtering transport in capacitive radio frequency discharges," Plasma Processes Polym. **14**, 1600140 (2017).
[21]Y. Yoshino, T. Makino, Y. Katayama, and T. Hata, "Optimization of zinc oxide thin film for surface acoustic wave filters by radio frequency sputtering," Vacuum **59**, 538–545 (2000).
[22]S. Schwyn, H. Lehmann, and R. Widmer, "Waveguiding epitaxial $LiNbO_3$ layers deposited by radio frequency sputtering," J. Appl. Phys. **72**, 1154–1159 (1992).
[23]M. Hiramatsu, K. Shiji, H. Amano, and M. Hori, "Fabrication of vertically aligned carbon nanowalls using capacitively coupled plasma-enhanced chemical vapor deposition assisted by hydrogen radical injection," Appl. Phys. Lett. **84**, 4708–4710 (2004).
[24]W. Huang, X. Wang, M. Sheng, L. Xu, F. Stubhan, L. Luo, T. Feng, X. Wang, F. Zhang, and S. Zou, "Low temperature PECVD SiN x films applied in OLED packaging," Mater. Sci. Eng. B **98**, 248–254 (2003).
[25]M. Orfert and K. Richter, "Plasma enhanced chemical vapor deposition of SiN-films for passivation of three-dimensional substrates," Surf. Coat. Technol. **116**, 622–628 (1999).
[26]S. Hamaguchi and M. Dalvie, "Microprofile simulations for plasma etching with surface passivation," J. Vac. Sci. Technol. A **12**, 2745–2753 (1994).
[27]J. Lim and S.-J. Yun, "Method for forming nitrogen-containing oxide thin film using plasma enhanced atomic layer deposition," U.S. patent 6,723,642 (2004).
[28]L. Banko, S. Ries, D. Grochla, M. Arghavani, S. Salomon, J. Pfetzing-Micklich, A. Kostka, D. Rogalla, J. Schulze, P. Awakowicz *et al.*, "Effects of the ion to growth flux ratio on the constitution and mechanical properties of $Cr_1 - x$-Al_x-N thin films," ACS Comb. Sci. **21**, 782–793 (2019).
[29]S. Ries, L. Banko, M. Hans, D. Primetzhofer, J. M. Schneider, A. Ludwig, P. Awakowicz, and J. Schulze, "Ion energy control via the electrical asymmetry effect to tune coating properties in reactive radio frequency sputtering," Plasma Sources Sci. Technol. **28**, 114001 (2019).
[30]M. Creatore, F. Palumbo, R. d'Agostino, and P. Fayet, "RF plasma deposition of SiO_2-like films: Plasma phase diagnostics and gas barrier film properties optimisation," Surf. Coat. Technol. **142**, 163–168 (2001).
[31]S. Steves, B. Ozkaya, C. Liu, O. Ozcan, N. Bibinov, G. Grundmeier, and P. Awakowicz, "Silicon oxide barrier films deposited on pet foils in pulsed plasmas: Influence of substrate bias on deposition process and film properties," J. Phys. D: Appl. Phys. **46**, 084013 (2013).
[32]M. Gebhard, F. Mitschker, C. Hoppe, M. Aghaee, D. Rogalla, M. Creatore, G. Grundmeier, P. Awakowicz, and A. Devi, "A combinatorial approach to enhance barrier properties of thin films on polymers: Seeding and capping of PECVD thin films by PEALD," Plasma Processes Polym. **15**, 1700209 (2018).
[33]C. Hoppe, F. Mitschker, P. Awakowicz, D. Kirchheim, R. Dahlmann, T. de los Arcos, and G. Grundmeier, "Adhesion of plasma-deposited silicon oxide barrier layers on PDMS containing polypropylene," Surf. Coat. Technol. **335**, 25–31 (2018).
[34]M. Tucci, L. Serenelli, S. De Iuliis, D. Caputo, A. Nascetti, and G. De Cesare, "Amorphous/crystalline silicon heterostructure solar cell based on multicrystalline silicon," in *Proceedings of 21st EUPVSEC, Dresden, Germany* (WIP Renewable Energies, 2006), Vol. 902.
[35]G. S. Oehrlein and S. Hamaguchi, "Foundations of low-temperature plasma enhanced materials synthesis and etching," Plasma Sources Sci. Technol. **27**, 023001 (2018).
[36]H. Profijt, S. Potts, M. Van de Sanden, and W. Kessels, "Plasma-assisted atomic layer deposition: Basics, opportunities, and challenges," J. Vac. Sci. Technol. A **29**, 050801 (2011).
[37]K. J. Kanarik, T. Lill, E. A. Hudson, S. Sriraman, S. Tan, J. Marks, V. Vahedi, and R. A. Gottscho, "Overview of atomic layer etching in the semiconductor industry," J. Vac. Sci. Technol. A **33**, 020802 (2015).
[38]M. Moravej, X. Yang, R. Hicks, J. Penelon, and S. Babayan, "A radio-frequency nonequilibrium atmospheric pressure plasma operating with argon and oxygen," J. Appl. Phys. **99**, 093305 (2006).
[39]N. Balcon, A. Aanesland, and R. Boswell, "Pulsed RF discharges, glow and filamentary mode at atmospheric pressure in argon," Plasma Sources Sci. Technol. **16**, 217 (2007).
[40]V. Schulz-Von Der Gathen, L. Schaper, N. Knake, S. Reuter, K. Niemi, T. Gans, and J. Winter, "Spatially resolved diagnostics on a microscale atmospheric pressure plasma jet," J. Phys. D: Appl. Phys. **41**, 194004 (2008).
[41]J. Waskoenig, K. Niemi, N. Knake, L. Graham, S. Reuter, V. Schulz-Von Der Gathen, and T. Gans, "Atomic oxygen formation in a radio-frequency driven micro-atmospheric pressure plasma jet," Plasma Sources Sci. Technol. **19**, 045018 (2010).
[42]T. Hemke, A. Wollny, M. Gebhardt, R. P. Brinkmann, and T. Mussenbrock, "Spatially resolved simulation of a radio-frequency driven micro-atmospheric pressure plasma jet and its effluent," J. Phys. D: Appl. Phys. **44**, 285206 (2011).
[43]R. Brandenburg, "Dielectric barrier discharges: Progress on plasma sources and on the understanding of regimes and single filaments," Plasma Sources Sci. Technol. **26**, 053001 (2017).

[44]J. T. Gudmundsson and D. I. Snorrason, "On electron heating in a low pressure capacitively coupled oxygen discharge," J. Appl. Phys. **122**, 193302 (2017).
[45]V. Georgieva, A. Bogaerts, and R. Gijbels, "Numerical study of Ar/CF_4/N_2 discharges in single-and dual-frequency capacitively coupled plasma reactors," J. Appl. Phys. **94**, 3748–3756 (2003).
[46]S. Segawa, M. Kurihara, N. Nakano, and T. Makabe, "Dependence of driving frequency on capacitively coupled plasma in CF_4," Jpn. J. Appl. Phys. **38**, 4416 (1999).
[47]Z. Donkó and Z. L. Petrović, "Analysis of a capacitively coupled dual-frequency CF_4 discharge," Jpn. J. Appl. Phys. **45**, 8151 (2006).
[48]A. Agarwal, S. Rauf, and K. Collins, "Gas heating mechanisms in capacitively coupled plasmas," Plasma Sources Sci. Technol. **21**, 055012 (2012).
[49]F. Hamaoka, T. Yagisawa, and T. Makabe, "Numerical investigation of relationship between micro-scale pattern, interfacial plasma structure and feature profile during deep-Si etching in two-frequency capacitively coupled plasmas in SF_6/O_2," J. Phys. D: Appl. Phys. **42**, 075201 (2009).
[50]B. Kwon, J. Kim, N.-E. Lee, and J. Shon, "Ultrahigh selective etching of SiO2 using an amorphous carbon mask in dual-frequency capacitively coupled C_4F_8/CH_2F_2/O_2/Ar plasmas," J. Electrochem. Soc. **157**, D135–D141 (2010).
[51]J. Coburn and E. Kay, "Positive-ion bombardment of substrates in rf diode glow discharge sputtering," J. Appl. Phys. **43**, 4965–4971 (1972).
[52]R. A. Gottscho, G. R. Scheller, D. Stoneback, and T. Intrator, "The effect of electrode area ratio on low-frequency glow discharges," J. Appl. Phys. **66**, 492–500 (1989).
[53]B. G. Heil, U. Czarnetzki, R. P. Brinkmann, and T. Mussenbrock, "On the possibility of making a geometrically symmetric RF-CCP discharge electrically asymmetric," J. Phys. D: Appl. Phys. **41**, 165202 (2008).
[54]B. Horváth, J. Schulze, Z. Donkó, and A. Derzsi, "The effect of electron induced secondary electrons on the characteristics of low-pressure capacitively coupled radio frequency plasmas," J. Phys. D: Appl. Phys. **51**, 355204 (2018).
[55]O. Braginsky, A. Kovalev, D. Lopaev, O. Proshina, T. Rakhimova, A. Vasilieva, D. Voloshin, and S. Zyryanov, "Experimental and theoretical study of dynamic effects in low-frequency capacitively coupled discharges," J. Phys. D: Appl. Phys. **45**, 015201 (2011).
[56]M. Radmilović-Radjenović and Z. L. Petrović, "Influence of the surface conditions on rf plasma characteristics," Eur. Phys. J. D **54**, 445–449 (2009).
[57]A. Derzsi, I. Korolov, E. Schüngel, Z. Donkó, and J. Schulze, "Effects of fast atoms and energy-dependent secondary electron emission yields in PIC/MCC simulations of capacitively coupled plasmas," Plasma Sources Sci. Technol. **24**, 034002 (2015).
[58]H. Hannesdottir and J. T. Gudmundsson, "On singlet metastable states, ion flux and ion energy in single and dual frequency capacitively coupled oxygen discharges," J. Phys. D: Appl. Phys. **50**, 175201 (2017).
[59]M. Daksha, A. Derzsi, S. Wilczek, J. Trieschmann, T. Mussenbrock, P. Awakowicz, Z. Donkó, and J. Schulze, "The effect of realistic heavy particle induced secondary electron emission coefficients on the electron power absorption dynamics in single-and dual-frequency capacitively coupled plasmas," Plasma Sources Sci. Technol. **26**, 085006 (2017).
[60]U. Kortshagen and L. D. Tsendin, *Electron Kinetics and Applications of Glow Discharges* (Springer Science & Business Media, 1998), Vol. 367.
[61]J. Schulze and T. Mussenbrock, "Electron heating in technological plasmas," Plasma Sources Sci. Technol. **25**, 020401 (2016).
[62]O. Popov and V. Godyak, "Power dissipated in low-pressure radio-frequency discharge plasmas," J. Appl. Phys. **57**, 53–58 (1985).
[63]V. Godyak and R. Piejak, "Abnormally low electron energy and heating-mode transition in a low-pressure argon rf discharge at 13.56 MHz," Phys. Rev. Lett. **65**, 996 (1990).
[64]V. Godyak, "Statistical heating of electrons at an oscillating plasma boundary," Sov. Phys.-Tech. Phys. (Engl. Transl.) **16**(7), 1073–1076 (1972).
[65]M. A. Lieberman, "Analytical solution for capacitive rf sheath," IEEE Trans. Plasma Sci. **16**, 638–644 (1988).
[66]M. A. Lieberman and V. A. Godyak, "From Fermi acceleration to collisionless discharge heating," IEEE Trans. Plasma Sci. **26**, 955–986 (1998).
[67]T. Lafleur, P. Chabert, M. Turner, and J.-P. Booth, "Equivalence of the hard-wall and kinetic-fluid models of collisionless electron heating in capacitively coupled discharges," Plasma Sources Sci. Technol. **23**, 015016 (2014).
[68]E. Fermi, "On the origin of the cosmic radiation," Phys. Rev. **75**, 1169 (1949).
[69]M. Turner and M. Hopkins, "Anomalous sheath heating in a low pressure rf discharge in nitrogen," Phys. Rev. Lett. **69**, 3511 (1992).
[70]M. M. Turner, "Collisionless heating in radio-frequency discharges: A review," J. Phys. D: Appl. Phys. **42**, 194008 (2009).
[71]T. Lafleur and P. Chabert, "Is collisionless heating in capacitively coupled plasmas really collisionless?," Plasma Sources Sci. Technol. **24**, 044002 (2015).
[72]D. Vender and R. Boswell, "Electron–sheath interaction in capacitive radio-frequency plasmas," J. Vac. Sci. Technol. A **10**, 1331–1338 (1992).
[73]B. P. Wood, see https://inis.iaea.org/search/search.aspx?orig_q=RN:26003961 for "Sheath heating in low-pressure capacitive radio frequency discharges" (1991).
[74]B. P. Wood, M. Lieberman, and A. Lichtenberg, "Stochastic electron heating in a capacitive rf discharge with non-Maxwellian and time-varying distributions," IEEE Trans. Plasma Sci. **23**, 89–96 (1995).
[75]M. Surendra and M. Dalvie, "Moment analysis of rf parallel-plate-discharge simulations using the particle-in-cell with Monte Carlo collisions technique," Phys. Rev. E **48**, 3914 (1993).
[76]T. Lafleur, P. Chabert, and J.-P. Booth, "Electron heating in capacitively coupled plasmas revisited," Plasma Sources Sci. Technol. **23**, 035010 (2014).
[77]R. P. Brinkmann, "Electron heating in capacitively coupled rf plasmas: A unified scenario," Plasma Sources Sci. Technol. **25**, 014001 (2015).
[78]T. Mussenbrock and R. P. Brinkmann, "Nonlinear electron resonance heating in capacitive radio frequency discharges," Appl. Phys. Lett. **88**, 151503 (2006).
[79]T. Mussenbrock and R. P. Brinkmann, "Nonlinear plasma dynamics in capacitive radio frequency discharges," Plasma Sources Sci. Technol. **16**, 377 (2007).
[80]Z. Donkó, J. Schulze, U. Czarnetzki, and D. Luggenhölscher, "Self-excited nonlinear plasma series resonance oscillations in geometrically symmetric capacitively coupled radio frequency discharges," Appl. Phys. Lett. **94**, 131501 (2009).
[81]S. Wilczek, J. Trieschmann, D. Eremin, R. P. Brinkmann, J. Schulze, E. Schuengel, A. Derzsi, I. Korolov, P. Hartmann, Z. Donkó *et al.*, "Kinetic interpretation of resonance phenomena in low pressure capacitively coupled radio frequency plasmas," Phys. Plasmas **23**, 063514 (2016).
[82]S. Wilczek, J. Trieschmann, J. Schulze, Z. Donkó, R. P. Brinkmann, and T. Mussenbrock, "Disparity between current and voltage driven capacitively coupled radio frequency discharges," Plasma Sources Sci. Technol. **27**, 125010 (2018).
[83]V. Godyak, "Steady-state low-pressure rf discharge," Sov. J. Plasma Phys. **2**, 78–84 (1976).
[84]U. Czarnetzki, T. Mussenbrock, and R. Brinkmann, "Self-excitation of the plasma series resonance in radio-frequency discharges: An analytical description," Phys. Plasmas **13**, 123503 (2006).
[85]T. Mussenbrock, R. Brinkmann, M. Lieberman, A. Lichtenberg, and E. Kawamura, "Enhancement of ohmic and stochastic heating by resonance effects in capacitive radio frequency discharges: A theoretical approach," Phys. Rev. Lett. **101**, 085004 (2008).
[86]M. Lieberman, A. Lichtenberg, E. Kawamura, T. Mussenbrock, and R. P. Brinkmann, "The effects of nonlinear series resonance on Ohmic and stochastic heating in capacitive discharges," Phys. Plasmas **15**, 063505 (2008).
[87]E. Schüngel, S. Brandt, Z. Donkó, I. Korolov, A. Derzsi, and J. Schulze, "Electron heating via self-excited plasma series resonance in geometrically symmetric multi-frequency capacitive plasmas," Plasma Sources Sci. Technol. **24**, 044009 (2015).
[88]B. Bora, H. Bhuyan, M. Favre, E. Wyndham, and H. Chuaqui, "Theoretical approach for plasma series resonance effect in geometrically symmetric dual radio frequency plasma," Appl. Phys. Lett. **100**, 094103 (2012).
[89]P. Saikia, H. Bhuyan, M. Escalona, M. Favre, B. Bora, M. Kakati, E. Wyndham, R. Rawat, and J. Schulze, "The electrical asymmetry effect in a multi frequency geometrically asymmetric capacitively coupled plasma: A study by a nonlinear global model," J. Appl. Phys. **123**, 183303 (2018).
[90]M. Turner, "Pressure heating of electrons in capacitively coupled rf discharges," Phys. Rev. Lett. **75**, 1312 (1995).

[91]M. Turner, D. Hutchinson, R. Doyle, and M. Hopkins, "Heating mode transition induced by a magnetic field in a capacitive rf discharge," Phys. Rev. Lett. **76**, 2069 (1996).
[92]G. Gozadinos, M. Turner, and D. Vender, "Collisionless electron heating by capacitive rf sheaths," Phys. Rev. Lett. **87**, 135004 (2001).
[93]J. Schulze, Z. Donkó, B. Heil, D. Luggenhölscher, T. Mussenbrock, R. Brinkmann, and U. Czarnetzki, "Electric field reversals in the sheath region of capacitively coupled radio frequency discharges at different pressures," J. Phys. D: Appl. Phys. **41**, 105214 (2008).
[94]J. Schulze, A. Derzsi, K. Dittmann, T. Hemke, J. Meichsner, and Z. Donkó, "Ionization by drift and ambipolar electric fields in electronegative capacitive radio frequency plasmas," Phys. Rev. Lett. **107**, 275001 (2011).
[95]J. Schulze, Z. Donkó, A. Derzsi, I. Korolov, and E. Schuengel, "The effect of ambipolar electric fields on the electron heating in capacitive rf plasmas," Plasma Sources Sci. Technol. **24**, 015019 (2014).
[96]S. Huang and J. T. Gudmundsson, "Dual-frequency capacitively coupled chlorine discharge," Plasma Sources Sci. Technol. **24**, 015003 (2014).
[97]Y.-X. Liu, Q.-Z. Zhang, W. Jiang, L.-J. Hou, X.-Z. Jiang, W.-Q. Lu, and Y.-N. Wang, "Collisionless bounce resonance heating in dual-frequency capacitively coupled plasmas," Phys. Rev. Lett. **107**, 055002 (2011).
[98]Y.-X. Liu, Q.-Z. Zhang, W. Jiang, W.-Q. Lu, and Y.-N. Wang, "Experimental validation and simulation of collisionless bounce-resonance heating in capacitively coupled radio-frequency discharges," Plasma Sources Sci. Technol. **21**, 035010 (2012).
[99]Y.-X. Liu, Q.-Z. Zhang, J. Liu, Y.-H. Song, A. Bogaerts, and Y.-N. Wang, "Effect of bulk electric field reversal on the bounce resonance heating in dual-frequency capacitively coupled electronegative plasmas," Appl. Phys. Lett. **101**, 114101 (2012).
[100]Y.-X. Liu, Q.-Z. Zhang, J. Liu, Y.-H. Song, A. Bogaerts, and Y.-N. Wang, "Electron bounce resonance heating in dual-frequency capacitively coupled oxygen discharges," Plasma Sources Sci. Technol. **22**, 025012 (2013).
[101]W. Jiang, H.-y. Wang, S.-x. Zhao, and Y.-n. Wang, "Hysteresis induced by gap length effects in capacitively coupled plasmas at low pressures," J. Phys. D: Appl. Phys. **42**, 102005 (2009).
[102]P. Belenguer and J. Boeuf, "Transition between different regimes of rf glow discharges," Phys. Rev. A **41**, 4447 (1990).
[103]J. Schulze, Z. Donkó, E. Schüngel, and U. Czarnetzki, "Secondary electrons in dual-frequency capacitive radio frequency discharges," Plasma Sources Sci. Technol. **20**, 045007 (2011).
[104]A. Derzsi, B. Horváth, I. Korolov, Z. Donkó, and J. Schulze, "Heavy-particle induced secondary electrons in capacitive radio frequency discharges driven by tailored voltage waveforms," J. Appl. Phys. **126**, 043303 (2019).
[105]I. B. Bernstein, J. M. Greene, and M. D. Kruskal, "Exact nonlinear plasma oscillations," Phys. Rev. **108**, 546 (1957).
[106]G. Gozadinos, D. Vender, M. Turner, and M. Lieberman, "Collisionless electron heating by capacitive radio-frequency plasma sheaths," Plasma Sources Sci. Technol. **10**, 117 (2001).
[107]D. O'Connell, T. Gans, D. Vender, U. Czarnetzki, and R. Boswell, "Plasma ionization through wave-particle interaction in a capacitively coupled radio-frequency discharge," Phys. Plasmas **14**, 034505 (2007).
[108]A. Meige, D. O'Connell, T. Gans, and R. Boswell, "Plasma ionization in low-pressure radio-frequency discharges—Part II: Particle-in-cell simulation," IEEE Trans. Plasma Sci. **36**, 1384–1385 (2008).
[109]S. Sharma and M. Turner, "Simulation study of wave phenomena from the sheath region in single frequency capacitively coupled plasma discharges; field reversals and ion reflection," Phys. Plasmas **20**, 073507 (2013).
[110]S. Sharma and M. Turner, "Investigation of wave emission phenomena in dual frequency capacitive discharges using particle-in-cell simulation," J. Phys. D: Appl. Phys. **47**, 285201 (2014).
[111]M. M. Turner and P. Chabert, "Collisionless heating in capacitive discharges enhanced by dual-frequency excitation," Phys. Rev. Lett. **96**, 205001 (2006).
[112]M. M. Turner and P. Chabert, "Electron heating mechanisms in dual-frequency capacitive discharges," Plasma Sources Sci. Technol. **16**, 364 (2007).
[113]I. Kaganovich, V. Demidov, S. Adams, and Y. Raitses, "Non-local collisionless and collisional electron transport in low-temperature plasma," Plasma Phys. Controlled Fusion **51**, 124003 (2009).
[114]V. Kolobov and V. Godyak, "Electron kinetics in low-temperature plasmas," Phys. Plasmas **26**, 060601 (2019).
[115]I. B. Bernstein and T. Holstein, "Electron energy distributions in stationary discharges," Phys. Rev. **94**, 1475 (1954).
[116]L. Tsendin, "Energy distribution of electrons in a weakly ionized current-carrying plasma with a transverse inhomogeneity," Sov. Phys. JETP **39**, 805–810 (1974).
[117]L. Tsendin, "Electron kinetics in non-uniform glow discharge plasmas," Plasma Sources Sci. Technol. **4**, 200 (1995).
[118]U. Kortshagen, C. Busch, and L. Tsendin, "On simplifying approaches to the solution of the Boltzmann equation in spatially inhomogeneous plasmas," Plasma Sources Sci. Technol. **5**, 1 (1996).
[119]V. Godyak, "Hot plasma effects in gas discharge plasma," Phys. Plasmas **12**, 055501 (2005).
[120]V. Vahedi, M. Lieberman, G. DiPeso, T. Rognlien, and D. Hewett, "Analytic model of power deposition in inductively coupled plasma sources," J. Appl. Phys. **78**, 1446–1458 (1995).
[121]I. Kaganovich, V. Kolobov, and L. Tsendin, "Stochastic electron heating in bounded radio-frequency plasmas," Appl. Phys. Lett. **69**, 3818–3820 (1996).
[122]Y. M. Aliev, I. Kaganovich, and H. Schlüter, "Quasilinear theory of collisionless electron heating in radio frequency gas discharges," Phys. Plasmas **4**, 2413–2421 (1997).
[123]T. Gans, V. Schulz-von der Gathen, and H. Döbele, "Prospects of phase resolved optical emission spectroscopy as a powerful diagnostic tool for rf-discharges," Contrib. Plasma Phys. **44**, 523–528 (2004).
[124]B. G. Heil, J. Schulze, T. Mussenbrock, R. P. Brinkmann, and U. Czarnetzki, "Numerical modeling of electron beams accelerated by the radio frequency boundary sheath," IEEE Trans. Plasma Sci. **36**, 1404–1405 (2008).
[125]J. Schulze, B. Heil, D. Luggenhölscher, R. Brinkmann, and U. Czarnetzki, "Stochastic heating in asymmetric capacitively coupled rf discharges," J. Phys. D: Appl. Phys. **41**, 195212 (2008).
[126]J. Schulze, B. Heil, D. Luggenhölscher, T. Mussenbrock, R. Brinkmann, and U. Czarnetzki, "Electron beams in asymmetric capacitively coupled radio frequency discharges at low pressures," J. Phys. D: Appl. Phys. **41**, 042003 (2008).
[127]J. Schulze, E. Schüngel, Z. Donkó, D. Luggenhölscher, and U. Czarnetzki, "Phase resolved optical emission spectroscopy: A non-intrusive diagnostic to study electron dynamics in capacitive radio frequency discharges," J. Phys. D: Appl. Phys. **43**, 124016 (2010).
[128]B. Berger, K. You, H.-C. Lee, T. Mussenbrock, P. Awakowicz, and J. Schulze, "Observation of the generation of multiple electron beams during a single sheath expansion phase in capacitive rf plasmas," Plasma Sources Sci. Technol. **27**, 12LT02 (2018).
[129]S. Wilczek, J. Trieschmann, J. Schulze, E. Schuengel, R. P. Brinkmann, A. Derzsi, I. Korolov, Z. Donkó, and T. Mussenbrock, "The effect of the driving frequency on the confinement of beam electrons and plasma density in low-pressure capacitive discharges," Plasma Sources Sci. Technol. **24**, 024002 (2015).
[130]B. Bruneau, T. Gans, D. O'Connell, A. Greb, E. V. Johnson, and J.-P. Booth, "Strong ionization asymmetry in a geometrically symmetric radio frequency capacitively coupled plasma induced by sawtooth voltage waveforms," Phys. Rev. Lett. **114**, 125002 (2015).
[131]D. Hoffman, "A sputtering wind," J. Vac. Sci. Technol. A **3**, 561–566 (1985).
[132]A. Bogaerts, R. Gijbels, and V. V. Serikov, "Calculation of gas heating in direct current argon glow discharges," J. Appl. Phys. **87**, 8334–8344 (2000).
[133]J. Lu and M. J. Kushner, "Effect of sputter heating in ionized metal physical vapor deposition reactors," J. Appl. Phys. **87**, 7198–7207 (2000).
[134]A. Fruchtman, "Neutral gas depletion in low temperature plasma," J. Phys. D: Appl. Phys. **50**, 473002 (2017).
[135]A. Bogaerts and R. Gijbels, "The role of fast argon ions and atoms in the ionization of argon in a direct-current glow discharge: A mathematical simulation," J. Appl. Phys. **78**, 6427–6431 (1995).

[136]A. Phelps and Z. L. Petrovic, "Cold-cathode discharges and breakdown in argon: Surface and gas phase production of secondary electrons," Plasma Sources Sci. Technol. **8**, R21 (1999).
[137]M. Lieberman, J. Booth, P. Chabert, J. Rax, and M. Turner, "Standing wave and skin effects in large-area, high-frequency capacitive discharges," Plasma Sources Sci. Technol. **11**, 283 (2002).
[138]P. Chabert, "Electromagnetic effects in high-frequency capacitive discharges used for plasma processing," J. Phys. D: Appl. Phys. **40**, R63 (2007).
[139]S. Pancheshnyi, S. Biagi, M. Bordage, G. Hagelaar, W. Morgan, A. Phelps, and L. Pitchford, "The LXCat project: Electron scattering cross sections and swarm parameters for low temperature plasma modeling," Chem. Phys. **398**, 148–153 (2012).
[140]L. Alves, "The IST-LISBON database on LXCat," in *Journal of Physics: Conference Series* (IOP Publishing, 2014), Vol. 565, p. 012007.
[141]L. C. Pitchford, L. L. Alves, K. Bartschat, S. F. Biagi, M.-C. Bordage, I. Bray, C. E. Brion, M. J. Brunger, L. Campbell, A. Chachereau *et al.*, "Lxcat: An open-access, web-based platform for data needed for modeling low temperature plasmas," Plasma Processes Polym. **14**, 1600098 (2017).
[142]Y. L. Klimontovich, *The Statistical Theory of Non-Equilibrium Processes in a Plasma*, International Series of Monographs in Natural Philosophy (Elsevier, 2013), Vol. 9.
[143]L. Pitchford, S. ONeil, and J. Rumble, Jr., "Extended Boltzmann analysis of electron swarm experiments," Phys. Rev. A **23**, 294 (1981).
[144]R. Robson and K. Ness, "Velocity distribution function and transport coefficients of electron swarms in gases: Spherical-harmonics decomposition of Boltzmann's equation," Phys. Rev. A **33**, 2068 (1986).
[145]E. A. Richley, "Elliptic representation of the Boltzmann equation with validity for all degrees of anisotropy," Phys. Rev. E **59**, 4533 (1999).
[146]D. Loffhagen and F. Sigeneger, "Advances in Boltzmann equation based modelling of discharge plasmas," Plasma Sources Sci. Technol. **18**, 034006 (2009).
[147]S. Dujko and R. White, "A multi term Boltzmann equation analysis of non-conservative electron transport in time-dependent electric and magnetic fields," in *Journal of Physics: Conference Series* (IOP Publishing, 2008), Vol. 133, p. 012005.
[148]V. I. Kolobov and R. R. Arslanbekov, "Simulation of electron kinetics in gas discharges," IEEE Trans. Plasma Sci. **34**, 895–909 (2006).
[149]Z. L. Petrović, Z. Raspopović, S. Dujko, and T. Makabe, "Kinetic phenomena in electron transport in radio-frequency fields," Appl. Surf. Sci. **192**, 1–25 (2002).
[150]L. Alves, A. Bogaerts, V. Guerra, and M. Turner, "Foundations of modelling of nonequilibrium low-temperature plasmas," Plasma Sources Sci. Technol. **27**, 023002 (2018).
[151]A. Sitenko and V. Malnev, *Plasma Physics Theory* (CRC Press, 1994), Vol. 10.
[152]S. Chapman, T. G. Cowling, and D. Burnett, *The Mathematical Theory of Non-uniform Gases: An Account of the Kinetic Theory of Viscosity, Thermal Conduction and Diffusion in Gases* (Cambridge University Press, 1990).
[153]K. H. Becker, U. Kogelschatz, K. Schoenbach, and R. Barker, *Non-equilibrium Air Plasmas at Atmospheric Pressure* (CRC Press, 2004).
[154]D. B. Graves and K. F. Jensen, "A continuum model of dc and rf discharges," IEEE Trans. Plasma Sci. **14**, 78–91 (1986).
[155]D. B. Graves, "Fluid model simulations of a 13.56-mhz rf discharge: Time and space dependence of rates of electron impact excitation," J. Appl. Phys. **62**, 88–94 (1987).
[156]S.-K. Park and D. J. Economou, "Analysis of low pressure rf glow discharges using a continuum model," J. Appl. Phys. **68**, 3904–3915 (1990).
[157]T. Makabe, N. Nakano, and Y. Yamaguchi, "Modeling and diagnostics of the structure of rf glow discharges in Ar at 13.56 MHz," Phys. Rev. A **45**, 2520 (1992).
[158]H. Kim, F. Iza, S. Yang, M. Radmilović-Radjenović, and J. Lee, "Particle and fluid simulations of low-temperature plasma discharges: Benchmarks and kinetic effects," J. Phys. D: Appl. Phys. **38**, R283 (2005).
[159]J. Van Dijk, G. Kroesen, and A. Bogaerts, "Plasma modelling and numerical simulation," J. Phys. D: Appl. Phys. **42**, 190301 (2009).
[160]T. N. An, E. Marode, and P. Johnson, "Monte Carlo simulation of electrons within the cathode fall of a glow discharge in helium," J. Phys. D: Appl. Phys. **10**, 2317 (1977).
[161]J. Boeuf and E. Marode, "Monte Carlo simulation of electron swarm motion in SF_6," J. Phys. D: Appl. Phys. **17**, 1133 (1984).
[162]G. Braglia and L. Romanò, "Monte Carlo and Boltzmann two-term calculations of electron transport in CO_2," Lettere al Nuovo Cimento (1971–1985) **40**, 513–518 (1984).
[163]V. Stojanovic and Z. L. Petrovic, "Comparison of the results of Monte Carlo simulations with experimental data for electron swarms in from moderate to very high electric field to gas density ratios," J. Phys. D: Appl. Phys. **31**, 834 (1998).
[164]J. Lawler and U. Kortshagen, "Self-consistent Monte Carlo simulations of the positive column of gas discharges," J. Phys. D: Appl. Phys. **32**, 3188 (1999).
[165]S. Dujko, Z. Raspopović, and Z. L. Petrović, "Monte Carlo studies of electron transport in crossed electric and magnetic fields in CF_4," J. Phys. D: Appl. Phys. **38**, 2952 (2005).
[166]Z. Donkó, K. Rozsa, and R. Tobin, "Monte Carlo analysis of the electrons' motion in a segmented hollow cathode discharge," J. Phys. D: Appl. Phys. **29**, 105 (1996).
[167]S. Longo, "Monte Carlo simulation of charged species kinetics in weakly ionized gases," Plasma Sources Sci. Technol. **15**, S181 (2006).
[168]C. K. Birdsall, "Particle-in-cell charged-particle simulations, plus Monte Carlo collisions with neutral atoms, PIC-MCC," IEEE Trans. Plasma Sci. **19**, 65–85 (1991).
[169]C. K. Birdsall and A. B. Langdon, *Plasma Physics via Computer Simulation* (CRC Press, 2018).
[170]R. Hockney and J. W. Eastwood, *Computer Simulation Using Particles* (McGraw-Hill, Inc., 1981).
[171]J. P. Verboncoeur, "Particle simulation of plasmas: Review and advances," Plasma Phys. Controlled Fusion **47**, A231 (2005).
[172]K. Matyash, R. Schneider, F. Taccogna, A. Hatayama, S. Longo, M. Capitelli, D. Tskhakaya, and F. Bronold, "Particle in cell simulation of low temperature laboratory plasmas," Contrib. Plasma Phys. **47**, 595–634 (2007).
[173]Z. Donkó, "Particle simulation methods for studies of low-pressure plasma sources," Plasma Sources Sci. Technol. **20**, 024001 (2011).
[174]Y. Weng and M. J. Kushner, "Method for including electron-electron collisions in Monte Carlo simulations of electron swarms in partially ionized gases," Phys. Rev. A **42**, 6192 (1990).
[175]G. Hagelaar, "Coulomb collisions in the Boltzmann equation for electrons in low-temperature gas discharge plasmas," Plasma Sources Sci. Technol. **25**, 015015 (2015).
[176]H. Skullerud, "The stochastic computer simulation of ion motion in a gas subjected to a constant electric field," J. Phys. D: Appl. Phys. **1**, 1567 (1968).
[177]S. Lin and J. Bardsley, "The null-event method in computer simulation," Comput. Phys. Commun. **15**, 161–163 (1978).
[178]A. V. Phelps, "The application of scattering cross sections to ion flux models in discharge sheaths," J. Appl. Phys. **76**, 747–753 (1994).
[179]M. M. Turner, "Kinetic properties of particle-in-cell simulations compromised by Monte Carlo collisions," Phys. Plasmas **13**, 033506 (2006).
[180]E. Erden and I. Rafatov, "Particle in cell/Monte Carlo collision method for simulation of rf glow discharges: Effect of super particle weighting," Contrib. Plasma Phys. **54**, 626–634 (2014).
[181]M. M. Turner, A. Derzsi, Z. Donkó, D. Eremin, S. J. Kelly, T. Lafleur, and T. Mussenbrock, "Simulation benchmarks for low-pressure plasmas: Capacitive discharges," Phys. Plasmas **20**, 013507 (2013).
[182]J. Schulze, T. Kampschulte, D. Luggenhölscher, and U. Czarnetzki, "Diagnostics of the plasma series resonance effect in radio-frequency discharges," in *Journal of Physics: Conference Series*, Vol. 86 (IOP Publishing, 2007), p. 012010.
[183]B. Bora, H. Bhuyan, M. Favre, E. Wyndham, H. Chuaqui, and M. Kakati, "Measurements of time average series resonance effect in capacitively coupled radio frequency discharge plasma," Phys. Plasmas **18**, 103509 (2011).
[184]R. P. Brinkmann, "Beyond the step model: Approximate expressions for the field in the plasma boundary sheath," J. Appl. Phys. **102**, 093303 (2007).

[185]J. Schulze, Z. Donkó, T. Lafleur, S. Wilczek, and R. P. Brinkmann, "Spatio-temporal analysis of the electron power absorption in electropositive capacitive rf plasmas based on moments of the Boltzmann equation," Plasma Sources Sci. Technol. **27**, 055010 (2018).
[186]Y.-R. Zhang, X. Xu, and Y.-N. Wang, "Fluid simulation for influence of metastable atoms on the characteristics of capacitively coupled argon plasmas," Phys. Plasmas **17**, 033507 (2010).
[187]S. Sharma, N. Sirse, M. Turner, and A. Ellingboe, "Influence of excitation frequency on the metastable atoms and electron energy distribution function in a capacitively coupled argon discharge," Phys. Plasmas **25**, 063501 (2018).
[188]G. Stancu, N. Brenning, C. Vitelaru, D. Lundin, and T. Minea, "Argon metastables in HiPIMS: Validation of the ionization region model by direct comparison to time resolved tunable diode-laser diagnostics," Plasma Sources Sci. Technol. **24**, 045011 (2015).
[189]Y. Liu, J.-P. Booth, and P. Chabert, "Plasma non-uniformity in a symmetric radiofrequency capacitively-coupled reactor with dielectric side-wall: A two dimensional particle-in-cell/Monte Carlo collision simulation," Plasma Sources Sci. Technol. **27**, 025006 (2018).
[190]J. Schulze, E. Schüngel, U. Czarnetzki, M. Gebhardt, R. P. Brinkmann, and T. Mussenbrock, "Making a geometrically asymmetric capacitive rf discharge electrically symmetric," Appl. Phys. Lett. **98**, 031501 (2011).
[191]E. Schüngel, J. Schulze, Z. Donkó, and U. Czarnetzki, "Power absorption in electrically asymmetric dual frequency capacitive radio frequency discharges," Phys. Plasmas **18**, 013503 (2011).
[192]J. Schulze, E. Schüngel, Z. Donkó, and U. Czarnetzki, "Excitation dynamics in electrically asymmetric capacitively coupled radio frequency discharges: Experiment, simulation, and model," Plasma Sources Sci. Technol. **19**, 045028 (2010).
[193]E. Schüngel, Z. Donkó, P. Hartmann, A. Derzsi, I. Korolov, and J. Schulze, "Customized ion flux-energy distribution functions in capacitively coupled plasmas by voltage waveform tailoring," Plasma Sources Sci. Technol. **24**, 045013 (2015).